View Article Online
View Journal

Materials
Advances

This article can be cited before page numbers have been issued, to do this please use: J. A. S. Shakil, S. P. Saikat, N. Bhattacharjee, Md. A. Rahman, S. Bhowmik, M. U. Khandaker, J. Uddin and F. I. Chowdhury, *Mater. Adv.*, 2026, DOI: 10.1039/D6MA00207B.

ROYAL SOCIETY
OF CHEMISTRY

rsc.li/materials-advances

View Article Online
DOI: 10.1039/D6MA00207B

ARTICLE

Received 00th January 20xx,
Accepted 00th January 20xx

DOI: 10.1039/x0xx00000x

Toward Efficient and Sustainable Perovskite Solar Cells: A Combined First-Principles and Device Simulation Study of $K_2LiGa(Cl/Br)_6$ for Photovoltaic Performance Optimization

Jubaer Ahmod Shakil[a†], Shassatha Paul Saikat[b†], Niloy Bhattacharjee[a], Md. Atikur Rahman[a], Shukanta Bhowmik[b*], Mayeen Uddin Khandaker[c*], Jamal Uddin[d*], Faisal Islam Chowdhury[a*]

This work employs an integrated computational framework combining density functional theory (DFT) and SCAPS-1D device simulations to investigate the lead-free double halide perovskites $K_2LiGaCl_6$ and $K_2LiGaBr_6$ as potential photovoltaic absorbers. First-principles calculations indicate that both compounds are structurally feasible in the cubic elpasolite phase and satisfy preliminary thermodynamic and mechanical stability criteria. The calculated GGA-PBE electronic structures reveal direct band-gap semiconducting behaviour, with band gaps of 2.53 eV for $K_2LiGaCl_6$ and 1.19 eV for $K_2LiGaBr_6$, indicating distinct optoelectronic application windows. Optical calculations show absorption coefficients on the order of 10^4 cm^{-1} in the visible range, while elastic-property analysis suggests mechanically soft and ductile behaviour with moderate anisotropy, features that may support thin-film device integration. SCAPS-1D simulations performed under optimized conditions indicate $K_2LiGaBr_6$ as the more favourable single-junction photovoltaic absorber, yielding a simulated power conversion efficiency of approximately 27.13% with favourable open-circuit voltage and fill factor. These results identify $K_2LiGaBr_6$ as a promising environmentally benign alternative to lead-based perovskites, and provide a rational multiscale design strategy for the development of sustainable, high-performance photovoltaic materials.

Introduction

Perovskite materials, named after the mineral $CaTiO_3$ and sharing its ABX_3 (where A and B are metal cations and X is the halide anion) crystal structure, have emerged as a versatile class of semiconductors for optoelectronic technologies [1-3]. Recently, lead-halide perovskites have attracted considerable attention for their potential in diverse applications, such as dielectric materials for multilayer ceramic capacitors [4], superconductors [5], catalysts [6], magnetic systems [7], as well as optoelectronic and thermoelectric devices [8,9]. Lead-halide perovskites comprising organic-inorganic constituents have demonstrated a rapid enhancement in power conversion efficiency, progressing from 3.8% to 25.2% within a decade [10]. Lead-based perovskites, including methylammonium lead iodide ($CH_3NH_3PbI_3$), formamidinium lead iodide ($FAPbI_3$), cesium lead iodide ($CsPbI_3$), methylammonium lead bromide ($CH_3NH_3PbBr_3$), and cesium lead bromide ($CsPbBr_3$), can be compositionally tuned to absorb different regions of the solar spectrum, enabling high photoconversion efficiencies (PCE) [11-15]. When integrated with complementary absorber layers in tandem architectures, these materials can further enhance power output, with theoretical efficiencies surpassing 33% [16]. The growing interest in organohalide perovskites for photovoltaic and light-emitting diode (LED) applications stems from their composition, which relies on abundant and low-cost elements, as well as their compatibility with diverse fabrication approaches, particularly solution-based deposition techniques [17,18]. Although perovskites have reached commercially viable efficiency levels, significant challenges remain, including scalability in large-scale manufacturing, poor moisture stability under outdoor conditions, and the severe environmental and health hazards associated with toxic lead (Pb) [19-21]. These challenges are being actively addressed through various research efforts, such as substituting organic components, lead cations, and/or halide anions to reduce toxicity and improve stability [22,23]. Recent DFT studies on $A_2MM'Cl_6$ and X_2YInO_6 double perovskites show that cation substitution and compositional engineering can systematically tune structural stability, band gaps, optical absorption, elastic response, and thermoelectric descriptors, supporting descriptor-based screening as an effective route for identifying lead-free energy materials [24-26]. In particular, replacing Pb^{2+} with other divalent cations possessing an electronic configuration similar to that of lead has been explored as a strategy to eliminate lead-related toxicity [27]. For example, Han et al. demonstrated a facile solution-phase

---

[a] Department of Chemistry, Faculty of Science, University of Chittagong, Chittagong-4331, Bangladesh.
[b] Department of Applied Chemistry and Chemical Engineering, Noakhali Science and Technology University, Noakhali, Bangladesh.
[c] Applied Physics and Radiation Technologies Group, CCDCU, School of Engineering and Technology, Sunway University, 47500 Bandar Sunway, Selangor, Malaysia.
[d] Center for Nanotechnology, Department of Natural Sciences, Coppin State University, MD, USA.
† Equal Contribution.

synthesis of lead-free Cs_2SnX_6(X = Br, I) with excellent structural stability and fabricated Cs_2SnI_6-based photodetectors exhibiting outstanding performance and durability [28]. On the other hand, Uddin et al. optimized lead-free $CsGeI_3$-based perovskite solar cells using SCAPS-1D, achieving a PCE of 25.16% with the FTO/TiO_2/$CsGeI_3$/CuO/Ni structure, highlighting the strong potential of germanium-based halide PSCs as efficient, non-toxic alternatives to Pb-based devices [29]. However, experimental studies have shown that Sn^{2+} and Ge^{2+} are prone to rapid oxidation to Sn^{4+} and Ge^{4+}, which leads to the instability of the corresponding perovskites [30,31].

Recently, numerous studies have explored all inorganic materials derived from double perovskites [32-34]. Double perovskites with the general formula $A_2MM'X_6$ (where A = alkali metal such as Na, K, Cs, or Rb; M = monovalent transition metal like Cu, Ag, or In; M′ = trivalent transition metal such as Bi, Sb, or Ga; and X = halide) have advanced significantly in incorporating diverse elements into their structure [35]. Consequently, combinations of monovalent (M^+) and trivalent (M'^{3+}) cations can serve as substitutes for the two divalent Pb^{2+} ions [36]. For instance, Filip et al. and McClure et al. investigated the band gap characteristics of lead-free halide double perovskites ($Cs_2BiAgCl_6$ and $Cs_2BiAgBr_6$) and novel semiconductors (Cs_2AgBiX_6, X = Br, Cl), respectively [37,38]. Additionally, Chrafih et al. investigated cubic Cs_2AgBiX_6 (X = Cl, Br, I) double perovskites, revealing their promising structural, optical, and thermodynamic properties for durable, non-toxic optoelectronic and photovoltaic applications [39]. Several other lead-free, Cs-based double perovskites, including $Cs_2AgInCl_6$, $Cs_2AgSbCl_6$, $Cs_2CuSbCl_6$, and $Cs_2AgFeCl_6$, exhibit tunable photoluminescence and adjustable optical properties [40-43]. Despite its advantages, the widespread use of Cs-based double perovskites in large-scale, low-cost PSCs is limited by the scarcity of Cs, which constitutes only 0.00019% of the Earth's crust, making it the 50th most abundant element. This limitation has prompted researchers to consider potassium (K) as a substitute, as it belongs to the same group as Cs and is far more abundant, comprising 2.6% of the Earth's crust - about 10,000 times more than Cs [44]. Consequently, replacing Cs with K enables the development of stable, eco-friendly, and cost-effective all-inorganic PSCs using Earth-abundant elements [45,46].

K-based double halide perovskites exhibit remarkable properties, including high carrier mobility, strong optical absorption, ease of fabrication, and long carrier diffusion lengths [47]. For instance, Manzoor et al. employed DFT with GGA+mBJ to study K_2AgXI_6 (X = Sb, Bi) double perovskites, revealing indirect band gaps of 0.7-1.2 eV, strong visible-region absorption, favorable density of states, and thermodynamic stability, indicating their promise for optoelectronic and thermoelectric applications [48]. Zanib et al. investigated K_2AgAsX_6 (X = Cl, Br) double perovskites using WIEN2k and BoltzTraP, revealing indirect band gaps of 2.1 and 1.6 eV, strong visible-light absorption, ductile mechanical behavior, and favorable thermoelectric properties, highlighting their potential for solar cell and thermoelectric applications [49]. Similarly, Al-Qaisi et al. used DFT simulations via WIEN2k to study K_2CuSbX_6 (X = Cl, Br, I) double perovskites, revealing indirect band gaps (1.12-0.43 eV), strong visible-light absorption, low lattice thermal conductivity, and high thermoelectric performance, highlighting their potential for optoelectronic and renewable energy applications [50]. Nevertheless, the studied systems face challenges due to their instability and suboptimal optoelectronic properties. Therefore, it is essential to pursue novel lead-free halide double perovskites that combine structural stability, non-toxicity, and enhanced optoelectronic performance.

In the present work, we perform density functional theory (DFT) calculations integrating with SCAPS-1D simulation to explore the structural, electronic, and optical properties of a new K-based double perovskite, K_2LiGaX_6 (X = Br, Cl), aiming to investigate the possibility of their applications in optoelectronics. This study aims to motivate experimental researchers to synthesize and investigate $K_2LiGa(Br/Cl)_6$ to deepen our understanding of its properties, and facilitate its practical use in optoelectronic applications, supporting the development of environmentally friendly alternatives.

Methodology

First-principles calculations

The first-principles calculations were performed using the Cambridge Serial Total Energy Package (CASTEP), which employs a plane-wave pseudopotential approach within the framework of density functional theory (DFT) [51,52]. The exchange-correlation energy was described utilizing the generalized gradient approximation (GGA) as delineated by Perdew-Burke-Ernzerhof (PBE), whereas the on-the-fly generated (OTFG) ultrasoft pseudopotentials were implemented to effectively address the electron-ion interactions [53,54]. A plane-wave cutoff energy of 700 eV was selected subsequent to comprehensive convergence testing to ensure that the numerical precision of total energy remains within 1 meV per atom.

For the integration over the Brillouin zone, the Monkhorst-Pack k-point sampling scheme was employed [55]. In the phase of structural optimization, an 8 × 8 × 8 k-point grid was implemented, which proved adequate to fulfill the necessary convergence criteria pertaining to energy and forces. To augment the precision in the assessment of the electronic structure and optical characteristics, a more refined 20 × 20 × 20 k-point mesh was subsequently utilized for the computations of the electronic density of states (DOS and PDOS) as well as the optical properties.

The geometric optimizations of $K_2LiGaCl_6$ and $K_2LiGaBr_6$ were conducted under conditions of zero external pressure, accompanied by simultaneous relaxation of both lattice parameters and atomic positions. The limited-memory-Broyden-Fletcher-Goldfarb-Shanno (LBFGS) minimization algorithm was utilized, and Pulay stress corrections were incorporated to mitigate errors associated with the finite basis set [56]. Rigid convergence criteria were established to ensure the reliability of the structural parameters, which included a total energy tolerance of 5.0×10^{-6} eV per atom, a maximum force

View Article Online
DOI: 10.1039/D6MA00207B

threshold of 0.01 eV Å^{-1}, a maximum stress tolerance of 0.02 GPa, and a maximum atomic displacement of 5.0×10^{-4} Å. The electronic self-consistent field (SCF) cycle was deemed converged at 5.0×10^{-7} eV per atom, permitting up to 100 SCF iterations to attain a high degree of accuracy in energy minimization. The FFT grid density was configured to "precise," and an augmentation charge density scaling factor of 1.5 was employed. All calculations were executed under non-spin-polarized conditions, as both halide double perovskites exhibit non-magnetic properties in their cubic elpasolite phase. Following the optimization of the equilibrium structures, elastic constants (Cij) were derived via finite strain theory [57]. The approach comprised four steps for each applied strain, while restricting the maximum stress amplitude to 0.003 GPa and the maximum atomic displacement to 0.001 Å to preserve linearity of the elastic response.

The electronic band structures were computed along high-symmetry directions of the $Fm\overline{3}m$ Brillouin zone, in conjunction with the total and partial density of states (TDOS and PDOS). The optical properties, encompassing the real and imaginary components of the dielectric function, refractive index, absorption coefficient, reflectivity, and energy-loss spectra, were derived utilizing the frequency-dependent dielectric response within the framework of the independent-particle approximation. While advanced approaches such as hybrid functionals (e.g., HSE06) or GW-based many-body perturbation techniques are known to yield more accurate band gap and optical predictions, their computational demands exceeded the resources available for the present work. Instead, the GGA-PBE functional was employed, which has consistently been shown in prior studies on halide double perovskites and related semiconductors to reproduce structural parameters reliably and to capture the essential electronic and optical trends with sufficient accuracy [58]. This balance between computational efficiency and predictive reliability renders PBE a practical and well-validated choice for the present work.

Photovoltaic device modelling and simulation

In the current study, SCAPS-1D (version 3.3.12) is employed to estimate solar cell parameters for the compounds under investigation, benefiting from this integrated modeling approach. The program consists of several panels that allow users to adjust parameters and evaluate results. The schematic diagram of the proposed device architecture of the FTO/TiO$_2$/K$_2$LiGa(Cl/Br)$_6$/HTL/Au solar cells is shown in **Figure 1**. The solar-cell simulations were performed under controlled SCAPS-1D conditions using AM1.5G illumination with an intensity of 1000 mW cm^{-2}. The operating temperature was first varied from 280 to 400 K to assess its effect on V_{OC}, J_{SC}, FF, and PCE. Since the highest simulated performance was obtained at 280 K, all subsequent optimization analyses were conducted at this temperature. To accurately represent the device's dynamic behavior, the simulation frequency is set to 1×6^{16} Hz**.** A voltage sweep from 0 to 1.50 V is used to thoroughly evaluate the device's performance under different operating conditions. These simulations are performed using SCAPS-1D, a powerful software widely recognized for modeling and optimizing solar cell structures. The parameters for the electron transport layer (ETL) and hole transport layer (HTL) are sourced from references 12-16 and are presented in **Table 1** and **Table 2**, along with the absorber layer parameters, while the interface defects of the absorber, absorber/HTL, and absorber/ETL are detailed in **Table 3**. Conduction and valence band offsets at TiO$_2$/absorber and absorber/HTL interfaces for K$_2$LiGaBr$_6$ and K$_2$LiGaCl$_6$-based devices derived from SCAPS-1D parameters are presented in **Table 4**.

Table 1: Material input parameters used in SCAPS-1D simulation for FTO, TiO$_2$ ETL, and K$_2$LiGa(Cl/Br)$_6$ absorber layers.

Parameter	**FTO** [59]	**TiO$_2$(ETL)** [59]	**K$_2$LiGaBr$_6$ (this work)**	**K$_2$LiGaCl$_6$ (this work)**
Thickness (nm)	200	50	Variable, 300–900	Variable, 300–900
Band gap, E_g (eV)	3.5	3.2	1.2	2.5
Electron affinity, χ (eV)	4	4	3.86	4
Relative dielectric permittivity, ε_r	9	100	4.70	3.67
Effective density of states, N_C (cm^{-3})	2.2×10^{18}	2×10^{21}	2.3×10^{18}	2.6×10^{18}
Effective density of states, N_V (cm^{-3})	1.8×10^{19}	1×10^{21}	5.8×10^{18}	6.1×10^{18}
Electron thermal velocity (cm s^{-1})	10^7	10^7	10^7	10^7
Hole thermal velocity (cm s^{-1})	10^7	10^7	10^7	10^7
Electron mobility (cm^2 V^{-1} s^{-1})	20	0.006	100	100
Hole mobility (cm^2 V^{-1} s^{-1})	10	0.006	100	100
Donor density (cm^{-3})	10^{18}	0	1×10^{10}	1×10^{10}
Acceptor density (cm^{-3})	0	5.06×10^{19}	0	0

View Article Online
DOI: 10.1039/D6MA00207B

Table 2: Material input parameters of different hole transport layers (HTLs) used in SCAPS-1D simulation.

Parameters	**Spiro-OMeTAD** [60]	**CNTs** [61]	**MEH-PPV** [62]	**MoS_2** [63]
Thickness (nm)	150	100	50	200
Band gap, E_g (eV)	2.9	1.74	2.1	1.29
Electron affinity, χ (eV)	2.2	3.87	2.8	4.2
Relative dielectric permittivity, ε_r	3	9	3	3
Effective density of states, N_C (cm^{-3})	2×10^{18}	2.2×10^{18}	2.5×10^{19}	2.2 × 1018
Effective density of states, N_V (cm^{-3})	1.8×10^{18}	1.8×10^{19}	2.5×10^{19}	1.9 × 1019
Electron thermal velocity (cm s^{-1})	10^7	10^7	10^7	10^7
Hole thermal velocity (cm s^{-1})	10^7	10^7	10^7	10^7
Electron mobility (cm^2 V^{-1} s^{-1})	10^{-4}	11	0.5×10^{-4}	100
Hole mobility (cm^2 V^{-1} s^{-1})	10^{-4}	11	0.5×10^{-4}	150
Donor density (cm^{-3})	0	0	0	0
Acceptor density (cm^{-3})	10^{18}	10^{19}	10^{15}	10^{17}

Table 3: Defect parameters used for the $K_2LiGaCl_6$/$K_2LiGaBr_6$ absorber layers and device interfaces in SCAPS-1D simulation.

Parameters	**Absorber**	**TiO_2/Absorber**	**Absorber/HTL**
Density of defect (cm^{-3})	1×10^{12}	1×10^{10}	1×10^{10}
Type of charge state	Single acceptor (-/0)	Neutral	Neutral
Capture cross section for electron and hole (cm^{-2})	1×10^{-16}	1×10^{-18}	1×10^{-18}
Level above VBM (eV)	0.1-0.5	0.1-0.4	0.1-0.4

Table 4: Conduction-band offsets (CBOs) and valence-band offsets (VBOs) at the TiO_2/K_2LiGaX_6 and K_2LiGaX_6/HTL interfaces derived from SCAPS-1D parameters., where X = Br or Cl.

Interface	**CBO (Br)**	**CBO (Cl)**	**VBO (Br)**	**VBO (Cl)**
TiO_2 / Absorber	-0.14	0.00	N/A	N/A
Absorber / Spiro-OMeTAD	N/A	N/A	-0.04	-1.44
Absorber / MEH-PPV	N/A	N/A	-0.16	-1.60
Absorber / MoS_2	N/A	N/A	-0.43	-1.99
Absorber / CNTs	N/A	N/A	-0.55	-2.11

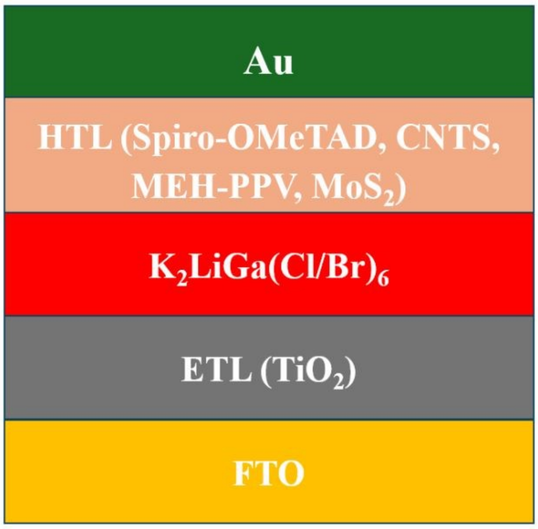

Figure 1: Schematic diagram of the solar cell device having $K_2LiGa(Cl/Br)_6$ lead free halide perovskites as an absorber layer.

Results and discussion

Structure and stability

Table 5: Optimized structural parameters of $K_2LiGa(Cl/Br)_6$ double halide perovskites.

Compounds	**Bond Lengths (Å)**	**Volume (Å³)**	**Density (g/cm³)**

View Article Online
DOI: 10.1039/D6MA00207B

	Lattice parameter (Å)	r_{Li-X}	r_{Ga-X}		
$K_2LiGaCl_6$	9.9622	2.9181	2.5264	988.70	2.4695
$K_2LiGaBr_6$	10.6315	3.1165	2.6426	1201.66	3.5061

The optimized geometric structure of $K_2LiGa(Cl/Br)_6$ halide double perovskites adopts a cubic symmetry that is classified under the $Fm\overline{3}m$ space group (No.225), as determined utilizing the PBE-GGA functional. This particular structure, shown in **Figure 2**, features a face-centered cubic lattice composed of alternating $[LiX6]^{5-}$ and $[GaX_6]^{3-}$ octahedra in a rock-salt-like arrangement, while the K^+ ions occupy the 12-fold coordinated A-sites between the octahedra [64,65]. In both of the compounds, the K^+ ions can be found occupying the 8c Wyckoff positions, which are specifically located at the fractional coordinates (¼, ¼, ¼), while the Li^+ ions are situated at the 4b positions corresponding to the coordinates (0, 0, ½), and Ga^{3+} ions reside at the 4a positions with the coordinates (0, 0, 0). Furthermore, the halide ions are arranged at the 24e sites characterized by fractional coordinates of the form (0, 0, z), with the specific z-values being measured at 0.24045 for Cl^- and 0.24171 for Br^-. The small difference in the halide z-coordinate reflects the larger ionic radius of Br^- compared with Cl^- and indicates a slight anion-position adjustment within the otherwise cubic framework.

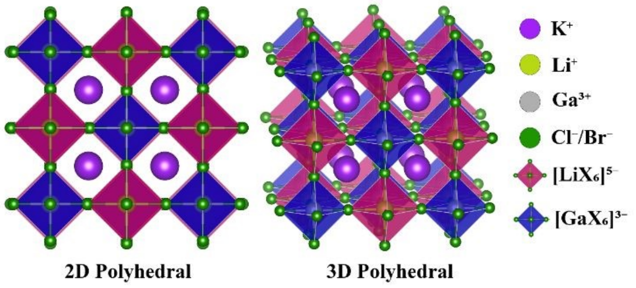

Figure 2: 2D and 3D polyhedral views of the cubic K_2LiGaX_6 (X = Cl, Br) double perovskite structure

As presented in **Table 5**, the optimized lattice parameter of $K_2LiGaCl_6$ has been ascertained to be 9.9622 Å, whereas $K_2LiGaBr_6$ demonstrates a larger value of 10.6315 Å. Consequently, the corresponding unit cell volume experiences an expansion from 988.70 Å³ for the chloride compound to 1201.66 Å³ for the bromide counterpart, a trend that aligns with the substitution of the larger Br^- ion in place of Cl^-. Notably, $K_2LiGaBr_6$ exhibits a significantly elevated density (3.5061 g/cm³) in comparison to $K_2LiGaCl_6$ (2.4695 g/cm³), despite the volumetric increase. This counterintuitive rise in density is primarily due to the greater atomic mass of bromine, which increases the overall mass of the unit cell more than the volume expansion offsets, thus leading to a net increase in density.

To assess the screening-level thermodynamic feasibility of $K_2LiGaCl_6$ and $K_2LiGaBr_6$, both the final ground-state energies and formation enthalpies were systematically evaluated. The final energies, obtained through DFT calculations, provide a measure of the overall energetic stability of each crystal structure, with more negative values indicating a lower energy configuration and, thus, a more stable system. As presented in **Table 6**, the calculated final energies for $K_2LiGaCl_6$ and $K_2LiGaBr_6$ are -648.28 eV/atom and -672.59 eV/atom, respectively. The more negative energy value associated with $K_2LiGaBr_6$ suggests that it possesses greater energetic stability compared to $K_2LiGaCl_6$, given the same computational parameters. Nonetheless, a direct comparison of final energies alone lacks significance owing to variations in total atomic composition and molar mass. A more pertinent metric is the formation enthalpy, determined utilizing Equation (1):

$$\Delta H_f = \frac{E_{K_2LiGaX_6} - (2E_K + E_{Li} + E_{Ga} + 6E_X)}{10} \qquad (1)$$

Here, $E_{K_2LiGaX_6}$ is the total energy of the compound (K_2LiGaX_6) per formula unit, and E_K, E_{Li}, E_{Ga}, and E_X denote the total energies of elemental potassium, lithium, gallium, and halogen (X = Cl or Br) in their most stable reference states, respectively [66].

The formation enthalpy was determined to be -1.5991 eV/atom for $K_2LiGaCl_6$ and -1.2811 eV/atom for $K_2LiGaBr_6$. The negative formation enthalpy values suggest that both compounds are energetically favourable with respect to their elemental constituents and therefore may be synthetically accessible. However, these values should be regarded as preliminary thermodynamic screening indicators rather than definitive proof of phase stability under operating conditions. The more negative value for $K_2LiGaCl_6$ indicates stronger thermodynamic favourability relative to $K_2LiGaBr_6$, which may be associated with shorter and stronger metal-halide bonds in the chloride variant. Specifically, the Li-Cl and Ga-Cl bond lengths are 2.9181 Å and 2.5264 Å, respectively, which are shorter than the corresponding Li-Br and Ga-Br bond lengths of 3.1165 Å and 2.6426 Å in $K_2LiGaBr_6$.

Table 6: Calculated stability descriptors and electronic band gaps of $K_2LiGa(Cl/Br)_6$ double halide perovskites.

Parameter	**$K_2LiGaCl_6$**	**$K_2LiGaBr_6$**
Total energy, $E_{tot.}$ (eV)	-25931.23	-26903.86
Energy per atom, E (eV/atom)	-648.28	-672.59
Formation enthalpy, ΔH_f (eV/atom)	-1.5991	-1.2811
Goldschmidt tolerance factor, τ	0.97	0.96
Global instability index, GII (v.u.)	0.0378	0.0615
Band gap, E_g (eV)	2.534	1.190

The Goldschmidt tolerance factor (τ) is a widely recognized parameter utilized to predict the structural stability and distortion tendencies of perovskite materials, defined by the following relationship [67]**:**

$$\tau = \frac{r_K + r_X}{\sqrt{2}\left(\frac{r_{Li} + r_{Ga}}{2} + r_X\right)}(2)$$

Where r_K, r_{Li}, r_{Ga}, and r_X represent the ionic radii of potassium, lithium, gallium, and the halide ion (Cl^- or Br^-), respectively. According to Goldschmidt's criterion, a tolerance factor approaching unity, typically within the interval $0.825 < \tau < 1.059$, indicates ideal ionic size compatibility that promotes the formation of stable cubic perovskite structures [68]. In this investigation, the two perovskite compounds $K_2LiGaCl_6$ and $K_2LiGaBr_6$ exhibit tolerance factors of 0.97 and 0.96, respectively, both of which lie firmly within the ideal range. This indicates a strong probability of structural stability and the formation of high-symmetry cubic phases for these halide perovskites, in alignment with empirical and theoretical observations reported for analogous halide materials[69,70].

The Global Instability Index (GII) functions as a quantitative metric that evaluates the overall structural integrity of a crystal by quantifying the deviations in bond lengths from their optimal values [71]. Specifically, it measures the extent to which calculated bond valence sums for individual atoms diverge from their formal oxidation states, thereby indicating the degree of bond-valence mismatch and internal lattice strain. Originally introduced by Brown and subsequently incorporated into structural prediction tools such as SPuDS, GII reflects the adherence of a structure to the electrostatic valence sum rule (VSR) [72,73]. This index is formally defined in Equation (3).

$$GII = \sqrt{\frac{\sum_{i=0}^{N}\left(V_i^{VSR} - V_i\right)^2}{N}}$$

Here, V_i^{VSR} represents the bond valence sum of atom *i* as predicted by the electrostatic valence sum rule (VSR), V_i denotes the formal oxidation state of atom *i*, and *N* is the total number of cations within the unit cell of the compound.

The GII value typically remains below 0.1 valence units (v.u.) for structures devoid of strain, whereas it may attain values as elevated as 0.2 v.u. when subjected to lattice-induced strains. Crystal structures that exhibit a GII exceeding 0.2 v.u. are often classified as unstable, and the documentation of such structures is generally considered to be flawed [74]. In the present investigation, the GII for $K_2LiGaBr_6$ and $K_2LiGaCl_6$ was computed utilizing the SPuDS program across all viable octahedral tilt configurations. The recorded minimal GII values (0.0378 for $K_2LiGaCl_6$ and 0.0615 for $K_2LiGaBr_6$) are indicative of a zero tilt angle, signifying an inclination towards the undistorted cubic ($a^oa^oa^o$) arrangement. This further implies that, although both structures remain within acceptable stability confines, the chloride variant may demonstrate enhanced stability and reduced distortion in comparison to its bromide counterpart.

Mechanical properties

The comprehension of the elastic characteristics of a material is crucial for forecasting its mechanical behavior in response to external forces, which consequently influences its suitability for structural, mechanical, and device-level implementations. Elastic constants (C_i▯) not only determine a material's ability to resist deformation but also reveal critical insights into interatomic bonding strength, ductility, brittleness, anisotropy, and overall mechanical stability [75]. In cubic crystal systems such as $K_2LiGa(Cl/Br)_6$, the mechanical properties are entirely characterized by three independent elastic stiffness coefficients, specifically C_{11}, C_{12}, and C_{44} [76]. The computed values of these elastic constants for $K_2LiGaCl_6$ (C_{11} = 35.48 GPa, C_{12} = 16.96 GPa, C_{44} = 14.63 GPa) and $K_2LiGaBr_6$ (C_{11} = 28.93 GPa, C_{12} = 13.84 GPa, C_{44} = 9.99 GPa) fulfill the mechanical stability prerequisites outlined by Born's stability criteria, which stipulate that $C_{11} > 0, C_{44} > 0, (C_{11} - C_{12}) > 0,\ and\ (C_{11} + 2C_{12}) > 0$ [77]. These conditions suggest that both compounds may possess sufficient mechanical integrity to maintain their cubic lattice configurations under applied mechanical stress.

In order to conduct a more comprehensive investigation into the mechanical resilience of these materials in response to various modes of deformation, secondary elastic parameters, such as the bulk modulus (B), shear modulus (G), and Young's modulus (Y), were calculated employing the Voigt-Reuss-Hill averaging methodology [78], as defined by the following equations.

$$B = \frac{C_{11} + 2C_{12}}{3}(4)$$

$$G_V = \frac{C_{11} - C_{12} + 3C_{44}}{5}(5)$$

$$G_R = \frac{5(C_{11} - C_{12})C_{44}}{3(C_{11} - C_{12}) + 4C_{44}}(6)$$

$$G = \frac{G_V + G_R}{2}(7)$$

$$E = \frac{9BG}{3B + G}(8)$$

$$\nu = \frac{3B - 2G}{2(3B + G)}(9)$$

In this context, V and R denote the Voigt and Reuss approximations, respectively. This averaging methodology effectively reconciles the upper (Voigt) and lower (Reuss) bounds of elastic behavior, thus facilitating a more precise assessment of the mechanical properties of polycrystalline materials. The calculated values of these parameters, alongside other mechanical descriptors such as Pugh's ratio (B/G), Poisson's ratio (ν), Cauchy's pressure, Lamé constant (λ), Debye temperature (θ_D), among other properties, are systematically tabulated in **Table 7**.

The bulk modulus (B), which serves as an indicator of a material's resistance to uniform compressive forces, has been determined to be 18.87 GPa for $K_2LiGaBr_6$ and 23.14 GPa for $K_2LiGaCl_6$, suggesting that the latter demonstrates enhanced incompressibility and greater volumetric stiffness. The shear modulus (G), which quantifies the material's ability to resist shape deformation under applied shear

View Article Online
DOI: 10.1039/D6MA00207B

stress, follows a similar trend, with values of 8.93 GPa for $K_2LiGaBr_6$ and 12.18 GPa for $K_2LiGaCl_6$. These relatively moderate G values indicate a mechanically soft nature in both compounds, which is beneficial for applications necessitating flexibility, such as the fabrication of thin films. [79]. Young's modulus (E), which quantitatively represents the stiffness or rigidity of a material subjected to linear deformation, is observed to be greater in $K_2LiGaCl_6$ (31.08 GPa) in comparison to its bromide analogue $K_2LiGaBr_6$ (23.14 GPa), thereby corroborating the assertion that $K_2LiGaCl_6$ exhibits enhanced resistance to elastic deformation. In alignment with these findings, the Lamé constant λ has been calculated to be 15.02 GPa for $K_2LiGaCl_6$ and 12.92 GPa for $K_2LiGaBr_6$, where the elevated value for the former material indicates a diminished compressibility and an augmented ability to endure volumetric strain. Collectively, these mechanical moduli suggest that while both compounds may display mechanical softness that is beneficial for flexible optoelectronic applications, $K_2LiGaCl_6$ is expected to be somewhat stiffer and more mechanically resilient than $K_2LiGaBr_6$.

Table 7: Computed elastic constants and derived mechanical properties of $K_2LiGa(Cl/Br)_6$ double halide perovskites.

Parameter	**$K_2LiGaCl_6$**	**$K_2LiGaBr_6$**
Elastic constant, C_{11} (GPa)	35.47	28.93
Elastic constant, C_{12} (GPa)	16.96	13.84
Elastic constant, C_{44} (GPa)	14.63	9.99
Shear modulus, G (GPa)	12.18	8.93
Bulk modulus, B (GPa)	23.13	18.87
Young's modulus, E (GPa)	31.08	23.14
Lamé constant, λ (GPa)	15.02	12.92
Pugh's Ratio, B/G	1.89	2.11
Poisson's Ratio, ν	0.27	0.29
Cauchy's Pressure, (GPa)	2.33	3.84
Kleinman Parameter, ξ	0.606	0.607
Average Sound Velocity, V_m (m/s)	2468.19	1782.76
Debye Temperature, θ_D (K)	251.89	170.48
Zener Anisotropy Factor, A	1.58	1.32
Universal Anisotropy Index, A^U	0.25	0.09

The evaluation of Pugh's ratio (B/G) and Poisson's ratio (ν) serves as a reliable approach to understanding a material's mechanical behavior, particularly in distinguishing between ductile and brittle characteristics under applied stress [80]. Pugh's criterion suggests that a material exhibits ductile behavior if the ratio of bulk modulus (B) to shear modulus (G) exceeds the critical threshold of 1.75, while materials with B/G < 1.75 are classified as brittle [81]. Similarly, Poisson's ratio offers insights into the material's capacity to undergo plastic deformation, with a critical value of 0.26 serving as the boundary between ductile (ν > 0.26) and brittle (ν < 0.26) behavior [82]. For $K_2LiGaBr_6$, the computed Pugh's ratio is 2.11, and the Poisson's ratio is 0.29. Both values are significantly above their respective threshold values, indicating a strong ductile nature. In comparison, $K_2LiGaCl_6$ also exhibits ductile characteristics, albeit to a somewhat lesser degree, with a Pugh's ratio of 1.89 and a Poisson's ratio of 0.27. The values for both halide double perovskites clearly surpass the critical thresholds (1.75 for B/G and 0.26 for ν), thereby confirming their ductile mechanical behavior.

When subjected to mechanical forces, a solid's stability can be influenced by either central or non-central interatomic forces. Poisson's ratio functions as a metric for determining the predominant type of force, with values ranging from 0.25 to 0.50 indicating central force solids that are predominantly stabilized by central forces, while values beyond this interval are indicative of non-central force solids that are stabilized by non-central forces [83]. Given that the Poisson's ratios of both compounds fall within the 0.25 to 0.50 range, they are classified as central force solids, implying that their structural integrity is predominantly dictated by central interatomic forces. Moreover, the Poisson's ratios are more closely aligned with the value of 0.33, which is characteristic of metallic bonding, as opposed to the 0.10 that is typical of covalent solids, thereby implying that the atomic interactions within these halide perovskites encompass a combination of covalent and metallic interactions, with a predominant metallic bonding character [84,85]. Additionally, Cauchy's pressure, defined as C_{12}–C_{44}, emerges as a significant parameter for deducing the nature of atomic bonding and the mechanical properties of materials [86]. Positive Cauchy's pressure values signify a predominance of ionic bonding and are generally correlated with ductile properties, whereas negative values are suggestive of covalent bonding and associated brittleness. In the present investigation, both $K_2LiGaBr_6$ and $K_2LiGaCl_6$ demonstrate positive Cauchy's pressure values, thereby affirming the predominance of ionic bonding and corroborating their ductile nature.

The Kleinman parameter (ζ), derived through the application of equation (5), serves as a quantifiable metric for the relative displacement of cationic and anionic sublattices during volume-conserving strain deformations, in the absence of constraints imposed by symmetry on atomic arrangement[87].

$$\zeta = \frac{C_{11} + 8C_{12}}{7C_{11} + 2C_{12}} (10)$$

This parameter delineates the internal strain state of the crystal, elucidating the comparative ease with which bond bending occurs relative to bond stretching, thereby inferring the lattice's resistance to angular changes induced by bending. The minimization of bond bending results in ζ=0, whereas the minimization of bond stretching yields ζ=1. In this investigation, ζ has been calculated to be 0.606 and 0.607 for $K_2LiGaCl_6$ and $K_2LiGaBr_6$, respectively, indicating that both materials exhibit a moderately balanced yet slightly preferred deformation response towards bond bending under applied strain.

The Debye temperature (θ_D) functions as a crucial parameter that interrelates the elastic properties of a material with its lattice dynamics and thermodynamic characteristics. It characterizes the

View Article Online
DOI: 10.1039/D6MA00207B

activation of phonons, which are quantized vibrational modes of the crystal lattice, and is frequently utilized to evaluate thermal transport, optical properties, and the applicability of materials for particular industrial uses. An elevated θ_D signifies the existence of higher-energy phonon modes, which typically serve to suppress the soft phonon modes that lack radiative relaxation, thus facilitating radiative phenomena such as photon emission. In contrast, a diminished θ_D generally denotes a greater prevalence of soft phonon modes, which promote non-radiative relaxation pathways that may impair optical efficiency [88]. This parameter is computed utilizing the following equation [89]:

$$\theta_D = \frac{h}{k}\left[\frac{3n}{4\pi}\left(\frac{N_A\rho}{M}\right)\right]^{\frac{1}{3}} V_m (11)$$

Where h denotes Planck's constant, k represents Boltzmann's constant, N_A is the Avogadro's number, n indicates the quantity of atoms per formula unit, M refers to the molecular mass per formula unit, ρ symbolizes the density, and V_m denotes the average sound velocity, formulated as [90]:

$$V_m = \left[\frac{1}{3}\left(\frac{2}{V_t^3} + \frac{1}{V_l^2}\right)\right]^{\frac{1}{3}} (12)$$

Here, the parameters V_l and V_t, referring to longitudinal and transverse elastic wave velocities respectively, are computed as follows [91]:

$$V_l = \sqrt{\frac{3B+4G}{3\rho}} \quad , \quad V_t = \sqrt{\frac{G}{\rho}} (13)$$

The obtained θ_D values, as illustrated in **Table 7**, indicate that $K_2LiGaCl_6$ presents a markedly higher Debye temperature (251.89 K) in comparison to $K_2LiGaBr_6$ (170.48 K). This observation aligns with the computed average sound velocities (V⍰), which are 2468.19 m/s and 1782.76 m/s, respectively. Such a correlation arises because θ_D is directly proportional to V⍰, which itself depends on the elastic moduli and density. The elevated θ_D in $K_2LiGaCl_6$ implies a more rigid lattice with increased phonon frequencies, potentially enhancing thermal conductivity and mechanical stability, while mitigating low-frequency soft phonon modes associated with non-radiative relaxation phenomena. Conversely, although $K_2LiGaBr_6$ displays a reduced θ_D, indicative of increased phonon scattering and softer vibrational modes, it may still demonstrate favorable performance in low-temperature operational conditions.

Anisotropic properties

In crystalline solids, the elastic and mechanical responses are frequently direction-dependent, a phenomenon referred to as elastic anisotropy. When the magnitude of an elastic property varies with crystallographic orientation, the material is deemed anisotropic; conversely, materials whose properties remain constant regardless of direction are classified as isotropic. In cubic crystals, the degree of anisotropy can be quantitatively described by the Zener anisotropy factor (A), expressed as [92]:

$$A = \frac{2C_{44}}{C_{11} - C_{12}}$$

For an ideal isotropic solid, A = 1. Any deviation from unity (A > 1 or A < 1) indicates elastic anisotropy. While A primarily reflects shear-related anisotropy, a more comprehensive assessment that accounts for both bulk and shear contributions is provided by the Universal Elastic Anisotropy Index (A^U), introduced by Ranganathan and Ostoja-Starzewski [93]:

$$A^U = 5\frac{G_V}{G_R} + \frac{B_V}{B_R} - 6$$

In the case of perfect isotropy, A^U=0; any non-zero, positive value is indicative of elastic anisotropy, with greater magnitudes representing increased directional variance. In the present study, the calculated A values for $K_2LiGaCl_6$ and $K_2LiGaBr_6$ are ascertained to be 1.5806 and 1.3252, respectively, both exceeding unity, thereby affirming the anisotropic properties of these perovskites. Nevertheless, the comparatively lower A value for $K_2LiGaBr_6$ suggests a diminished extent of shear-related anisotropy in contrast to its chloride equivalent. This assertion is supported by the A^U values, which are quantified as 0.25593 and 0.09577 for $K_2LiGaCl_6$ and $K_2LiGaBr_6$, respectively. The elevated A^U value for $K_2LiGaCl_6$ indicates a more significant divergence from isotropy, whereas the latter demonstrates a relatively more isotropic mechanical behavior.

To investigate the directional variation of elastic moduli in greater detail, the anisotropic elastic behavior of $K_2LiGaCl_6$ and $K_2LiGaBr_6$ was investigated using the ELATE program, which derives directional mechanical properties from the second-order elastic stiffness tensor (C⍰⍰) obtained via DFT calculations. In this method, the compliance tensor S_{ij}, obtained as the inverse of the stiffness tensor C_{ij}, is contracted with appropriate unit direction vectors over a continuous distribution of orientations in three-dimensional space to compute the spatial variation of Young's modulus E, shear modulus G, and Poisson's ratio ν. Extremal values for each modulus are then identified, and the degree of anisotropy is quantified by the ratio $A_X = X_{max}/X_{min}$, where X is E, G, or ν [94].

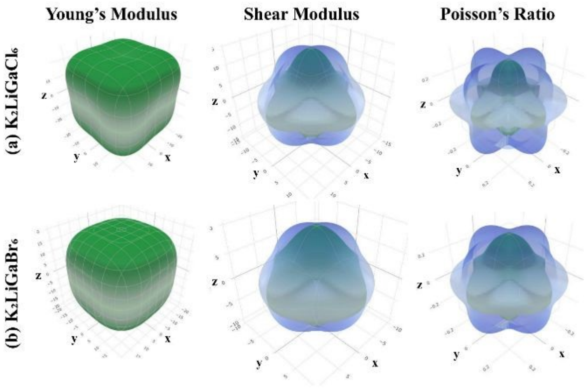

View Article Online
DOI: 10.1039/D6MA00207B

Figure 3: Directional dependence of Young's modulus, shear modulus, and Poisson's ratio for (a) $K_2LiGaCl_6$ and (b) $K_2LiGaBr_6$. Data computed using the ELATE program based on DFT-derived elastic tensors.

The three-dimensional (3D) surface plots of Young's modulus, shear modulus, and Poisson's ratio for both $K_2LiGaCl_6$ and $K_2LiGaBr_6$ are presented in **Figure 3**. These plots, produced utilizing the ELATE software, elucidate the manner in which each elastic property fluctuates with respect to crystallographic orientation. In an ideally isotropic material, such 3D surfaces would appear as perfect spheres, reflecting uniform mechanical response in all directions. Any deviation from this spherical form is suggestive of elastic anisotropy. The 3D representations depicted in **Figure 3** distinctly illustrate these deviations, with the surface of $K_2LiGaCl_6$ exhibiting a more pronounced distortion from spherical symmetry, thereby emphasizing its increased directional dependence when compared to $K_2LiGaBr_6$.The corresponding maximum and minimum values for each modulus, along with the anisotropy ratios that quantify these variations, are listed in **Table 8**.

According to the presented data, for $K_2LiGaCl_6$, the Young's modulus ranges from 24.50 to 36.25 GPa, resulting in an anisotropy ratio (A_E) of 1.48, in contrast to the more constrained range of 19.97 to 25.49 GPa and a lower A_E of 1.27 observed for $K_2LiGaBr_6$, thereby indicating a pronounced variation in stiffness contingent upon crystallographic orientation. A comparable pattern is discerned in the shear modulus, wherein $K_2LiGaCl_6$ displays values ranging from 9.25 to 14.63 GPa (A_G = 1.58), surpassing the 7.54 to 9.99 GPa range and A_G of 1.32 identified for $K_2LiGaBr_6$. The divergence is further emphasized by Poisson's ratio, as $K_2LiGaCl_6$ exhibits an extensive range of 0.106 to 0.427, alongside a notably heightened anisotropy ratio (A_v = 4.02) when compared with the narrower range of 0.192 to 0.386 and an A_v of 2.01 observed in $K_2LiGaBr_6$.

Altogether, the analysis of extremal values, the anisotropy indices, and the 3D surface plots consistently indicates that $K_2LiGaCl_6$ exhibits greater elastic anisotropy than $K_2LiGaBr_6$, both in magnitude and directional variation across all evaluated moduli. Such anisotropy bears significant practical implications: while moderate anisotropy may enhance mechanical adaptability in specific crystallographic orientations, excessive anisotropy has the potential to induce susceptibility to directional fracture.

Table 8: Directional elastic moduli and anisotropy ratios for $K_2LiGa(Cl/Br)_6$ double halide perovskites.

Perovskites	**Young's modulus (GPa)**			**Shear modulus (GPa)**			**Poisson's ratio**		
	E_{min}	E_{max}	A_E	G_{min}	G_{max}	A_G	ν_{min}	ν_{max}	A_{υ}
$K_2LiGaCl_6$	24.50	36.25	1.48	9.25	14.63	1.58	0.106	0.427	4.02
$K_2LiGaBr_6$	19.97	25.49	1.27	7.54	9.99	1.32	0.192	0.386	2.01

Electronic properties

In computational physics, the band structure shows how electronic energy levels change with crystal momentum in the Brillouin zone [95,96]. Researchers need this essential diagram because it gives them important information about many properties, such as electrical conductivity, absorption characteristics, photovoltaic performance, and how well the material works for certain uses [97,98]. **Figure 4** illustrates calculated band structure and TDOS plots of the novel inorganic double perovskite compounds $K_2LiGa(Cl/Br)_6$ examined in this study. Energy values are represented along the vertical axis, ranging from -6 to 6 eV, with the Fermi level (E_F) established at 0 eV. Whereas, the horizontal axis of the band structure plot shows the path through the Brillouin zone. For the creation energy-efficient solar cells and photovoltaic applications direct bandgap is an important parameter [99,100]. Both $K_2LiGaCl_6$ and $K_2LiGaBr_6$ exhibit a distinct direct band gap semiconducting material behavior. **Figure 4** shows that the VBM and CBM coincide at the Γ-point in reciprocal space. This alignment facilitates direct electronic transitions upon photon absorption and enables efficient electron-hole pair generation. There is no need for phonon assistance. Using GGA-PBE approximation, a comparatively smaller bandgap of 1.190 eV is seen for $K_2LiGaBr_6$ whereas $K_2LiGaCl_6$ showed a bandgap value of 2.534 eV. Br substitution has increased ionic radii which displaced the CBM towards fermi energy level and consequently diminishing the bandgap value of 1.344 eV for $K_2LiGaBr_6$ compared to $K_2LiGaCl_6$. This observation is consistent with prior findings in halide perovskites [101]. The perovskite materials that have lower bandgap values shows reduced UV photosensitivity and avoids wavelength cutoff in the UV region [102]. Therefore, UV detectors should have large bandgap value which is displayed by $K_2LiGaCl_6$. So, $K_2LiGaBr_6$ with its direct and smaller bandgap is optimal for solar cell applications while due to larger bandgap of $K_2LiGaCl_6$, it can be used in high-performance UV detection.

Moreover, we look more closely at the electronic properties by calculating the Total Density of States (TDOS) and splitting it down into its parts using the Partial Density of States (PDOS) (**Figure 5**).

View Article Online
DOI: 10.1039/D6MA00207B

This joint approach gives us a complete picture of how different energy states are filled and, most importantly, helps measure how much each orbital contributes to the overall band structure. To change the properties of a material for use in photocatalysis or photovoltaics, it is important to know how each atom interacts at the band edges. The TDOS analysis confirms the electronic structure calculations, which show that both $K_2LiGaCl_6$ and $K_2LiGaBr_6$ have semiconducting properties. The electronic band gap (E_g) in the band structure is accurate since there is a considerable forbidden energy region where the DOS drops to zero near the Fermi level. A look at the overall TDOS configuration shows that electronic states are spread out across the valence and conduction energy regions. This information confirms that the material is fundamentally suitable for generating and moving charge carriers when photons are absorbed. Also implemented the PDOS to get an improved comprehension of the material's electronic properties. The examination of the VBM reveals that its formation is primarily due to orbital contributions from the Cl/Br p states. The PDOS also shows that the s and p states of the A-site cation (K) and the M-site cation (Li) are close to the Fermi level, which helps define the VBM. On the other hand, the s orbitals of the Gallium cation (Ga) and the p orbitals of the Cl/Br atoms in both compounds mostly control the CBM. The Ga and halide orbitals are the most important, but the K and Li orbital states contribute to making the CB manifold.

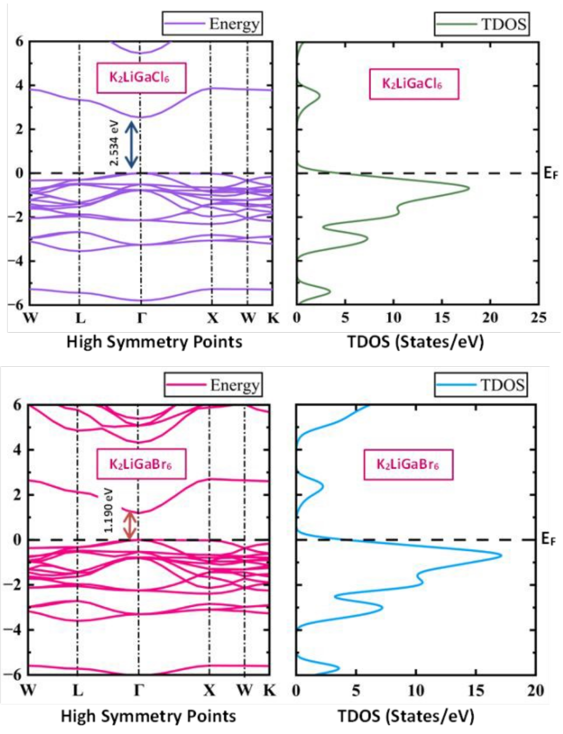

Figure 4: Calculated electronic band structures and TDOS of $K_2LiGaCl_6$ and $K_2LiGaBr_6$.

Optical properties

The optical response of a semiconductor is determined by its electronic band structure and the allowed inter-band transitions. These transitions govern how photons are absorbed, reflected or transmitted, directly affecting the material's suitability for optoelectronic devices and solar cells [103]. In particular, a material must absorb sunlight efficiently to serve as a good solar absorber or photodetector; for example, lead-free perovskites that exhibit absorption coefficients on the order of 10^4-10^5 cm^{-1} in the visible range are known to provide excellent light-trapping capabilities [104]. Thus, we have computed and analyzed the full spectrum of linear optical functions for the double-halide perovskites $K_2LiGa(Cl/Br)_6$. The studied properties include the absorption coefficient α(ω), reflectivity R(ω), refractive index n(ω), complex dielectric function, optical conductivity σ(ω), energy-loss function, and extinction coefficient. These parameters were evaluated across the photon-energy range of 0-5 eV to fully characterize the light-matter interactions in these compounds, with the corresponding results presented in **Figure 6.**

Dielectric function $\varepsilon(\omega)$

The complex dielectric function $\varepsilon(\omega)$ is the fundamental optical descriptor from which all linear optical constants are derived; it thus provides the natural starting point for any optical analysis [105]. By definition,

$$\varepsilon(\omega) = \varepsilon_1(\omega) + i\,\varepsilon_2(\omega),$$

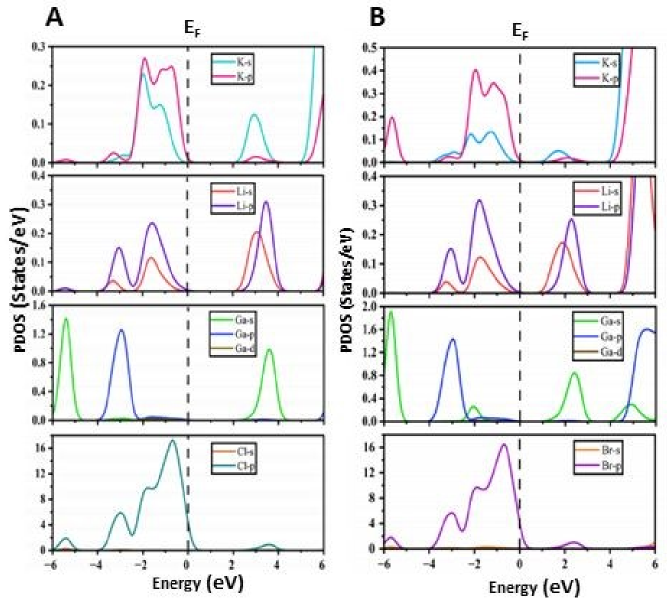

Figure 5: Orbital-projected partial density of states (PDOS) for **(A)** $K_2LiGaCl_6$ and **(B)** $K_2LiGaBr_6$.

where $\varepsilon_1(\omega)$ is the dispersive (real) part that quantifies the material's polarizability under an external electromagnetic field, and $\varepsilon_2(\omega)$ is the absorptive (imaginary) part that directly reflects allowed interband transitions. Physically, $\varepsilon_2(\omega)$ arises from the probability-weighted sum over electronic transitions between occupied and

View Article Online
DOI: 10.1039/D6MA00207B

unoccupied states, incorporating transition matrix elements and the Fermi-Dirac occupation factors [106]. The real part, $\varepsilon_1(\omega)$, is then obtained from $\varepsilon_2(\omega)$ via the Kramers-Kronig relation [107]:

$$\varepsilon_1(\omega) = 1 + \frac{2}{\pi}\,\mathcal{P}\int_0^{\infty} \frac{\omega'\,\varepsilon_2(\omega')}{\omega'^2 - \omega^2}\,d\omega',$$

where $\mathcal{P}$ denotes the principal value integral. Because the dielectric function $\varepsilon(\omega)$ encodes both dispersion and absorption, it is the source for the refractive index $n(\omega)$, extinction coefficient $k(\omega)$, absorption coefficient $\alpha(\omega)$, reflectivity $R(\omega)$ and the energy-loss function $L(\omega)$.

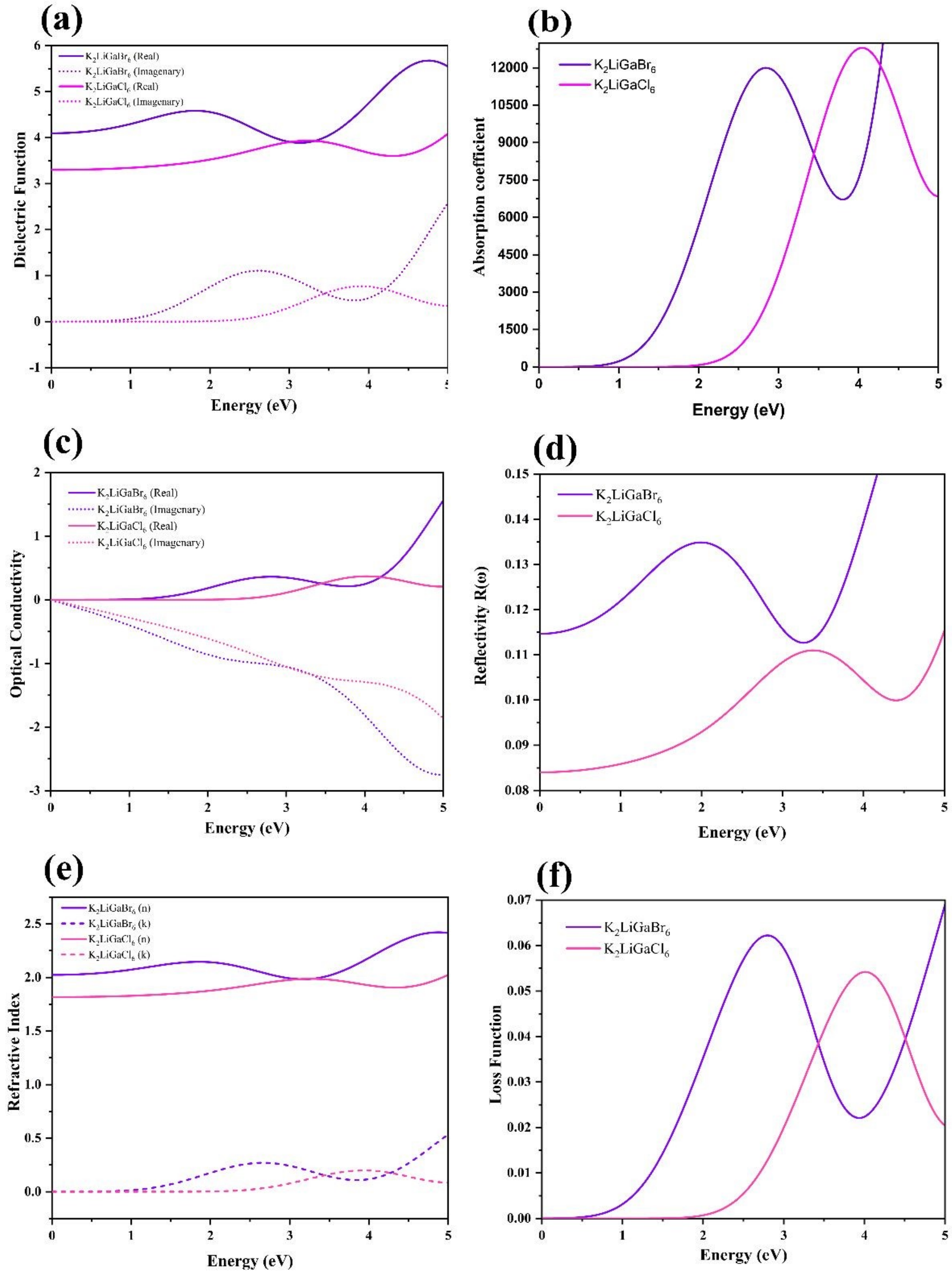

Figure 6: Graphical representations of **(a)** dielectric function (real and imaginary parts), **(b)** absorption, **(c)** conductivity (real and imaginary part), **(d)** refractive index and extinction coefficient, **(e)** reflectivity, and **(f)** Loss function for double perovskites $K_2LiGa(Cl/Br)_6$.

View Article Online
DOI: 10.1039/D6MA00207B

Figure 6(a) displays the calculated dielectric spectra for $K_2LiGaBr_6$ and $K_2LiGaCl_6$ across the photon-energy range of 0-5 eV. Both materials exhibit a marked increase in $\varepsilon_2(\omega)$ at their respective absorption edges, followed by secondary peaks at higher energies corresponding to other available interband transitions (e.g., from deeper halide p-states to conduction-band states dominated by Ga) [105], [108]. Specifically, the principal maxima in $\varepsilon_2(\omega)$ are located near 2.62 eV (with a value ~1.11) for $K_2LiGaBr_6$ and around 3.91 eV for $K_2LiGaCl_6$, which corresponds well to the difference in their band-gap magnitudes. The real part $\varepsilon_1(\omega)$ exhibits resonance-type maxima at low-to-moderate photon energies before decreasing at higher energies [109]; the calculated peak values are $\varepsilon_1 \approx 4.59$ for $K_2LiGaBr_6$ (around 1.81 eV) and $\varepsilon_1 \approx 3.93$ for $K_2LiGaCl_6$ (around 3.24 eV). Extrapolating to zero frequency yields static permittivities $\varepsilon_1(0)$ of approximately 4.1 (Br) and 3.3 (Cl). The relatively high static dielectric constants indicate strong Coulombic screening of photo-generated charge carriers, leading to a reduction in exciton binding energies and a suppression of non-radiative electron-hole recombination. Such characteristics are highly advantageous for enhancing the efficiency and stability of photovoltaic absorber materials [110]. Importantly, $\varepsilon_1(\omega)$ remains positive across the examined energy window for both materials, indicating dielectric behaviour in the visible range and only approaching zero at higher energies where collective (plasmonic) effects may arise.

From a device-perspective, the spectral placement and magnitude of the dielectric-function features have straightforward implications. The Br-containing compound, with its ε_2 peaks in the visible region and higher ε_1 at low-energy, is expected to show strong light absorption and good dielectric screening under solar illumination, making it the more promising candidate for single-junction photovoltaic applications. By contrast, the Cl-variant's dielectric response is shifted toward higher photon energies, suggesting better utility in UV sensing or blue-light optoelectronics rather than as a broadband solar absorber.

Absorption coefficient $\alpha(\omega)$

The absorption coefficient $\alpha(\omega)$ quantifies a material's ability to remove photons from a propagating beam and is therefore a direct metric of light-harvesting potential in optoelectronic and photovoltaic devices [111]. In our calculations, the absorption coefficient α(ω) remains negligible below the optical threshold, confirming the material's transparency within the sub-band-gap region, as illustrated in **Figure 6(b)**. A pronounced increase is observed at the absorption edge, corresponding to the onset of interband electronic transitions. This behavior mirrors the imaginary part of the dielectric function $\varepsilon_2(\omega)$ and validates the consistency between the computed band structure and optical spectra, since the absorption onset closely matches the DFT band gaps. The sharp rise in α(ω) beyond the band edge is a characteristic feature of halide perovskites and plays a vital role in thin-film photovoltaic design, since a high absorption coefficient minimizes the thickness of the active layer needed for effective light harvesting. For conventional perovskites, absorption coefficients exceeding 10^4 cm^{-1} near the band edge are routinely reported and are considered a practical benchmark for good light trapping [112-114]. Specifically, $K_2LiGaBr_6$ displays a prominent absorption peak of $\sim 1.20 \times 10^4$ cm^{-1} at approximately 2.83 eV (blue region), while $K_2LiGaCl_6$ reaches $\sim 1.28 \times 10^4$ cm^{-1} at near 4.04 eV (UV). The Br-based compound exhibits an absorption onset within the visible range, and its absorption coefficient surpasses 10^4 cm^{-1}, implying that thin films as thin as ~100 nm are sufficient to absorb a significant portion of incident solar radiation. This property is highly advantageous for thin-film photovoltaic applications. Although some high-absorption double perovskites have reported even larger α values (up to 10^5-10^6 cm^{-1} in certain spectral ranges), the magnitude observed here for $K_2LiGaBr_6$ is nonetheless significant for a lead-free halide system and places it among promising candidates for visible-light harvesting [115]. The spectral shape of $\alpha(\omega)$ typically shows an initial steep rise at the fundamental band edge followed by additional peaks corresponding to higher-energy transitions involving deeper valence bands. In both compounds the principal absorption features align with transitions from halogen-derived valence states into Ga-dominated conduction states, consistent with the orbital composition revealed by our band-structure analysis. Since optical conductivity σ(ω) is directly related to photon absorption, enhanced absorption leads to a larger population of excited carriers. Accordingly, the peaks observed in α(ω) are mirrored by corresponding increases in σ(ω), reinforcing the anticipated "photon-to-carrier" conversion efficiency that is typical of semiconductors. Such correlations between $\alpha(\omega)$, $\varepsilon_2(\omega)$ and $\sigma(\omega)$ are widely reported in theoretical and experimental studies of lead-free double perovskites and underscore the reliability of using computed optical spectra to screen new absorber materials [116,117]. From an application perspective, $K_2LiGaBr_6$ appears better suited for single-junction solar cells or visible photodetectors, whereas the Cl-analogue may be more appropriate for UV sensing or for optoelectronic devices that require wide-gap materials. Future work should refine these predictions with many-body corrections and consider excitonic effects and defect states that can modulate the effective absorption in real films [118].

Optical conductivity σ(ω)

View Article Online
DOI: 10.1039/D6MA00207B

Optical conductivity, σ(ω), reflects a material's ability to transport charge carriers in response to incident electromagnetic radiation. In the context of semiconductors and halide perovskites, it is directly correlated with the generation and mobility of photogenerated electrons and holes, and thus serves as a key parameter in evaluating materials for optoelectronic and photovoltaic applications [119,120]. The real part, $\sigma_1(\omega)$, represents the dissipative component, which corresponds to the actual movement of charge carriers and the resulting electrical conduction. On the other hand, the imaginary part $\sigma_2(\omega)$, is associated with energy storage and release during the oscillatory motion of charges [121,122].

From **Figure 6(c)**, the real part of the optical conductivity, $\sigma_1(\omega)$, shows well-defined peaks in the UV-visible spectral range, consistent with the onset of interband electronic transitions. For $K_2LiGaBr_6$, $\sigma_1(\omega)$ attains a maximum value of approximately 0.363 (1/fs) at 2.80 eV, while $K_2LiGaCl_6$ exhibits a slightly higher peak of about 0.37 (1/fs) at 4.01 eV. These maxima coincide with the high-absorption regions observed in the α(ω) spectra, indicating that photon absorption above the band gap effectively excites electrons into the conduction band, thereby enhancing conductivity. The nonzero σ_1 values even near the band edge confirm that both materials can generate mobile carriers when illuminated with photons of sufficient energy. The $\sigma_2(\omega)$ spectra reveal additional information about the dielectric response and energy dissipation mechanisms. For both perovskites, $\sigma_2(\omega)$ is negative at low photon energies before transitioning to positive values in the UV range. This crossover reflects the increasing dominance of interband transitions and free-carrier effects at higher energies. Notably, $K_2LiGaBr_6$, with its smaller band gap, shows a σ_1 peak in the lower-energy visible range, suggesting superior absorption and carrier generation under sunlight compared to $K_2LiGaCl_6$, which requires higher-energy (UV) photons to reach it2s conductivity peak. In practical terms, the Br-based compound could be more effective for single-junction solar cells, while the Cl-based material might find niche applications in UV photodetectors or multi-junction devices where higher-energy photon capture is desirable. The relationship between the absorption coefficient α(ω) and optical conductivity σ(ω) is a defining feature of semiconductor optoelectronic behavior, where photon absorption directly results in carrier generation and a corresponding rise in conductivity. This relationship, also reported in lead-free double perovskites such as $Cs_2AgInCl_6$ and $Cs_2AgInBr_6$ [115], underlines the potential of $K_2LiGaBr_6$ in thin-film photovoltaic architectures, where high absorption and photoconductivity can be achieved in layers only a few hundred nanometers thick.

Reflectivity R(ω)

Reflectivity R(ω) quantifies the fraction of incident light that is reflected by a material's surface an essential measure for assessing how much light is lost before absorption. In photovoltaic and optoelectronic contexts, low reflectivity over the operational spectrum is highly desirable, as it enhances photon capture and device efficiency [123].

In **Figure 6(d)**, we present the reflectivity spectra for $K_2LiGaBr_6$ and $K_2LiGaCl_6$ across the photon energy range. At near-zero photon energy, both materials demonstrate modest baseline reflectivity approximately 0.11 for the bromide and 0.08 for the chloride variant. These values remain low throughout the visible spectrum. Notably, $K_2LiGaBr_6$ peaks at around 0.135 near 1.99 eV, while $K_2LiGaCl_6$ peaks at approximately 0.111 near 3.37 eV. Such low reflectivity indicates that the majority of incident light successfully enters the material rather than being prematurely reflected. This property is shared with other promising lead-free double perovskites such as $Cs_2AgInCl_6$ and $Cs_2AgBiBr_6$, which pair low reflectivity with strong absorption to yield high photovoltaic potential [115].

From a physical perspective, the reflectivity remains low until photon energies approach a region where the real part of the dielectric function, $\varepsilon_1(\omega)$, approaches zero. At this plasmon resonance threshold, R(ω) rises sharply, a typical behavior for dielectric materials lacking free carriers. Below this point, light primarily enters the material to be absorbed or transmitted rather than reflected [106].

Low reflectivity in the visible range is a fundamentally favorable trait for solar absorbers and optoelectronic devices, as it maximizes light harvesting. Many high-performance device designs build upon this principle by incorporating high-index materials to trap and retain light within thin active layers, enhancing absorption beyond what would be achievable in a single pass [107]. Indeed, perovskites with higher refractive indices demonstrate improved light confinement, further amplifying absorption efficiency [107]. The reflectivity behavior of both $K_2LiGaBr_6$ and $K_2LiGaCl_6$ supports their candidacy as efficient light absorbers. The combination of low reflectivity across the visible range, particularly for $K_2LiGaBr_6$, along with strong absorption in that region, suggests that $K_2LiGaBr_6$ may be especially well suited for solar cell applications, while $K_2LiGaCl_6$ may find niche utility in near-UV optoelectronic devices.

Refractive index n(ω) and extinction coefficient k(ω)

The wavelength-dependent optical response of the double-halide perovskites $K_2LiGaBr_6$ and $K_2LiGaCl_6$ is characterized by their refractive index n(ω) and extinction coefficient k(ω), as shown in **Figure 6(e)**. At zero photon energy, the static refractive indices are calculated to be approximately 2.02 for $K_2LiGaCl_6$ and 1.52 for $K_2LiGaCl_6$. These values increase to well-defined peaks of $n \approx 2.146$ at 1.84 eV for the Br compound and $n \approx 1.987$ at 3.27 eV for the Cl compound, aligning with the moderate refractive indices commonly reported for halide perovskites, such as $MAPbI_3$, which shows $n \approx 2.6$ at 633 nm [124].

The extinction coefficient k(ω), a direct indicator of optical absorption strength, also displays sharp peaks approximately

View Article Online
DOI: 10.1039/D6MA00207B

k≈0.270 at 2.65 eV for $K_2LiGaBr_6$ and k≈0.198 at 3.94 eV for $K_2LiGaCl_6$.This optical behavior follows from the dielectric formalism where $2n(\omega)\,k(\omega)=\varepsilon_2(\omega)$, and the similarity in spectral trends underscores the causative influence of interband transitions in shaping both the absorption and refractive properties [105].

From a device-engineering standpoint, the moderate refractive indices in the visible suggest that $K_2LiGaBr_6$ and $K_2LiGaCl_6$ can effectively confine light with minimal reflection, thereby enhancing optical throughput in photovoltaic or photonic architectures. More so, the rapid rise in extinction coefficient near the band edge reveals robust absorption characteristics, reinforcing their potential for efficient light-harvesting applications.

Energy-loss function L(ω)

The energy-loss function, *L(ω)*, describes the energy dissipation experienced by an electromagnetic wave as it propagates through a material, primarily arising from inelastic scattering, heating, and plasmon excitation processes. It is mathematically defined as $L(\omega)=\mathrm{Im}[-1/\epsilon(\omega)]$, where $\varepsilon(\omega)$ is the complex dielectric function. This parameter serves as a sensitive probe of a material's dielectric response over different energy ranges, and is particularly useful for distinguishing behavior in the low-energy (visible) and high-energy (UV) regimes.

From **Figure 6(f)**, the peaks in L(ω) coincide with the photon energies at which the real part of the dielectric function $\varepsilon_1(\omega)$ crosses zero, a characteristic indicator of plasmon resonance. At these energies, the dielectric function transitions from positive to negative, signifying a shift from a predominantly reflective to an absorptive optical regime. In halide perovskites, such plasmon resonances are often linked to collective oscillations of the free or weakly bound electron population and are typically observed in the UV range. The modest magnitude and UV localization of these peaks suggest that $K_2LiGaBr_6$ and $K_2LiGaCl_6$ possess favorable optical loss characteristics for photovoltaic and optoelectronic applications. Specifically, their low visible-range losses imply that photons in the solar spectrum can be efficiently absorbed, enhancing their potential as absorber layers in solar cells. Furthermore, the presence of well-defined, yet weak, plasmon features could enable additional functionalities in plasmonic-assisted light trapping or photonic devices without introducing excessive parasitic absorption.

SCAPS-1D simulation

Effect of different HTL

An appropriate band gap and high hole mobility are essential requirements for effective hole transport layers (HTLs) [125]. In this study, four HTL materials - Spiro-OMeTAD, CNTS, MEH-PPV, and MoS_2 - were examined to evaluate their impact on the photovoltaic performance of the device, as shown in **Figure 7**. All simulations were conducted using TiO_2 as the electron transport layer (ETL). Among the investigated HTLs **(Table 9)**, MEH-PPV exhibited superior performance in the Au/MEH-PPV/$K_2LiGaBr_6$/TiO_2/FTO device structure, achieving a power conversion efficiency of approximately 27.13%. In addition, MEH-PPV demonstrated favorable energy level alignment with $K_2LiGaBr_6$, attributed to its suitable band gap of 1.19 eV. This alignment minimizes energy losses at the absorber/HTL interface, enhances hole extraction, and improves hole injection efficiency, collectively leading to enhanced device performance.

Table 9: Comparative photovoltaic performance of Au/HTL/K_2LiGaX_6/TiO_2/FTO solar cell structures, where X = Br or Cl.

HTL	V_{OC} (V)		J_{SC} (mA/cm²)		FF (%)		PCE (%)	
	$K_2LiGaBr_6$	$K_2LiGaCl_6$	$K_2LiGaBr_6$	$K_2LiGaCl_6$	$K_2LiGaBr_6$	$K_2LiGaCl_6$	$K_2LiGaBr_6$	$K_2LiGaCl_6$
Spiro-OMeTAD	0.985	1.1	33.157	25.8	82.81	83.1	27.05	23.6
CNTs	0.979	1.09	33.183	25.85	82.65	82.9	26.88	23.35
MEH-PPV	0.988	1.11	33.186	25.95	82.72	83.2	27.13	24
MoS_2	0.983	1.1	33.173	25.9	82.68	83	26.99	23.75

View Article Online
DOI: 10.1039/D6MA00207B

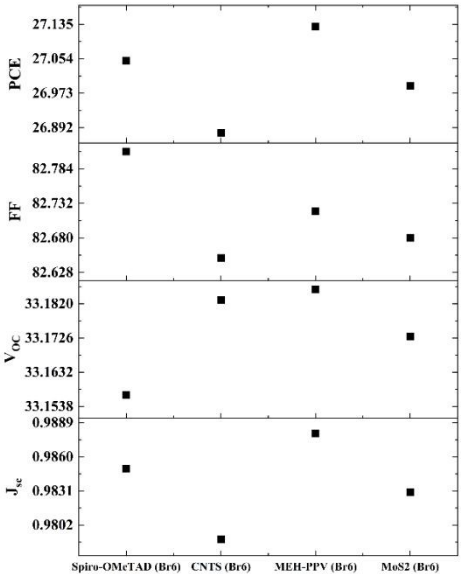

Figure 7: Effect of different HTLs on the performance of Voc, Jsc, FF, and PCE of $K_2LiGaBr_6$-based solar cells

HTLs play a vital role in selectively extracting holes from the perovskite absorber toward the cathode while simultaneously blocking electron transport. For an HTL to be viable for solar cell applications, it should satisfy several key criteria: (i) intrinsically high hole mobility, (ii) appropriate energy level alignment with the valence band of the perovskite, (iii) good photochemical and thermal stability along with solution processability, and (iv) efficient hole transport capability [60]. Proper energy level alignment facilitates efficient charge transfer across interfaces and suppresses recombination losses. Furthermore, high carrier mobility enables rapid transport of charge carriers to the electrodes, preventing charge accumulation that could otherwise lead to recombination. Therefore, careful selection of both ETL and HTL materials is critical, as their properties govern the built-in electric field that drives efficient charge separation and extraction within the device.

J-V characteristics

Figure 8(a) presents the simulated current density-voltage (J-V) characteristics of double-halide perovskite solar cells employing $K_2LiGaCl_6$ and $K_2LiGaBr_6$ absorber layers under standard illumination. Both devices exhibit a typical photovoltaic response, delivering high photocurrent densities in the low-bias region, followed by a gradual reduction in current magnitude as the applied voltage increases toward the open-circuit condition. The $K_2LiGaCl_6$-based device demonstrates a slightly higher short-circuit current density (J_{SC}≈32 mA/cm^2) compared to $K_2LiGaBr_6$ (J_{SC}≈30 mA/cm^2), suggesting improved photogeneration or absorption contribution in the chloride-based composition. In contrast, the $K_2LiGaBr_6$ device shows a higher voltage extension before the current approaches zero, indicating an enhanced open-circuit voltage and potentially reduced recombination losses. As the applied voltage reaches the high-bias region, the current density for both devices decrease toward zero due to increased carrier recombination and a reduced driving force for charge extraction. While $K_2LiGaCl_6$-based absorber supports higher photocurrent generation, $K_2LiGaBr_6$-based absorber delivers improved voltage characteristics. Such a trade-off may make the latter more advantageous for efficient device operation, as voltage gains are often critical for maximizing power conversion efficiency.

View Article Online
DOI: 10.1039/D6MA00207B

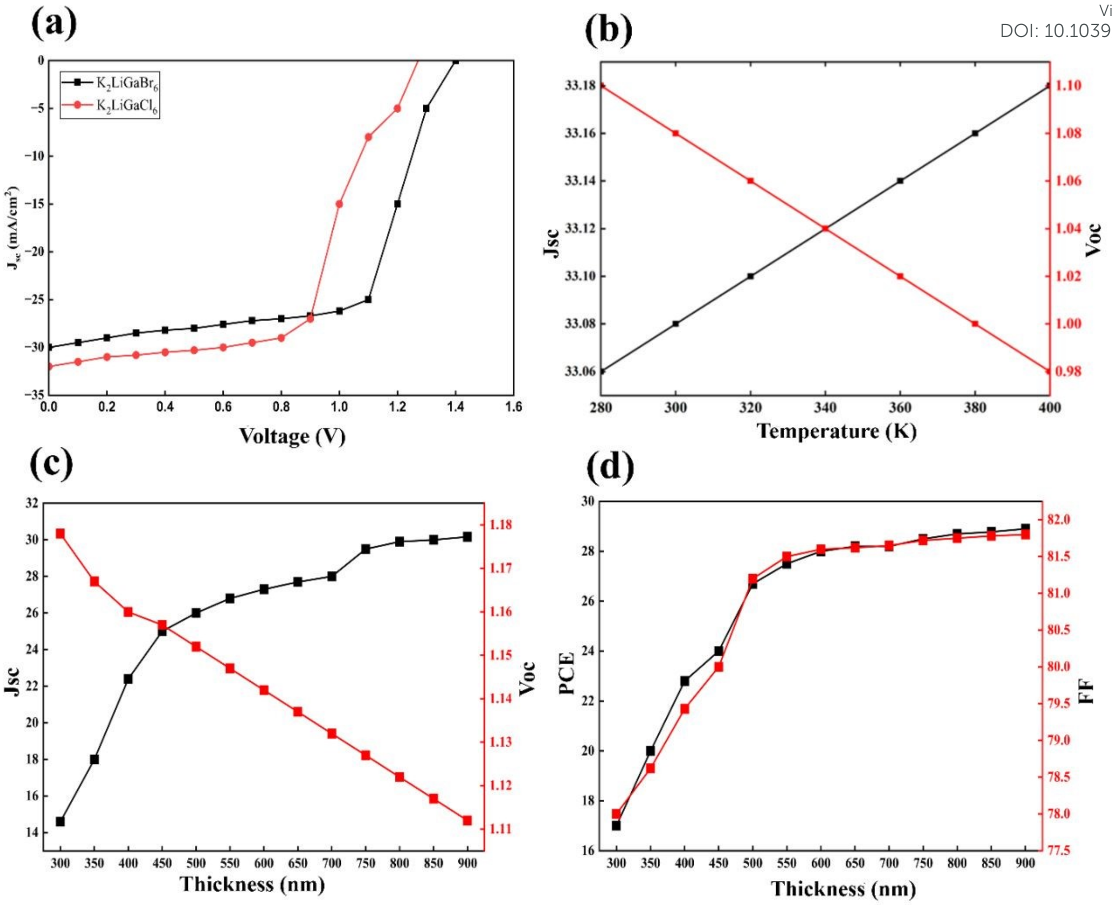

Figure 8: (a) current density-voltage J-V characteristics of $K_2LiGa(Br/Cl)_6$ solar cells, **(b)** variation of J_{SC} and V_{OC} with temperature for the $K_2LiGaBr_6$-based device, **(c)** effect of absorber-layer thickness on J_{SC} and V_{OC} for the $K_2LiGaBr_6$-based device, and **(d)** effect of absorber-layer thickness on PCE and FF for the $K_2LiGaBr_6$-based device.

Effect of working temperature

A fundamental step in assessing solar cell performance is the standard laboratory measurement of power conversion efficiency. However, under real operating conditions, solar cells are exposed to diverse environmental influences, including fluctuations in solar irradiance, temperature, and atmospheric conditions [126]. Such factors can significantly affect both the efficiency and long-term stability of solar cells, particularly those based on perovskite solar cell (PSC) technology. **Figure 8(b)** demonstrates the influence of temperature variation on $K_2LiGa(Cl/Br)_6$ performance, where the device temperature was varied from 280 to 400 K. A clear decline in the open-circuit voltage (V_{OC}) indicates the strong temperature dependence of this parameter. In contrast, the short-circuit current density (J_{SC}) shows an enhancement at elevated temperatures. This increase can be attributed to improved light absorption in the perovskite layer at higher temperatures, leading to increased generation of electron-hole pairs. Nevertheless, elevated temperatures also promote recombination processes and alter charge-carrier lifetimes, which can either positively or negatively impact device performance [127]. The combined effect of these competing mechanisms results in an overall reduction in device efficiency at higher temperatures. The optimum performance, with V_{OC} = 0.988 V, J_{SC} = 33.186 mA cm^{-2}, FF = 82.72%, and PCE = 27.13%, is achieved at 280 K. Consequently, this temperature was selected for subsequent analyses.

Effect of absorber layer thickness

The light-harvesting layer is a critical component of double halide perovskite solar cells, as it absorbs incident solar photons and generates charge carriers in the form of electrons and holes [63]. During device operation, holes are transported to the hole transport layer (HTL) while electrons are collected by the electron transport layer (ETL), enabling current flow through the external circuit. In this work, the thickness of the $K_2LiGaBr_6$ absorber layer was varied from 300 nm to 900 nm to investigate its influence on V_{OC}, J_{SC}, FF, and PCE. As shown in **Figure 8(c),** increasing the absorber thickness from 300 to 900 nm leads to a significant rise in the short-circuit current density (J_{SC}), which increases from approximately 14.5 mA/cm^2 to nearly 30 mA/cm^2. This improvement is mainly attributed to enhanced photon absorption and higher carrier generation in thicker absorber layers. In contrast, the open-circuit voltage (V_{OC}) gradually decreases from about 1.18 V to 1.11 V with increasing thickness, which can be explained by increased bulk recombination losses and longer carrier transport pathways in thicker films[61]. **Figure 8(d)** presents the corresponding variation of power conversion efficiency (PCE) and fill factor (FF). The PCE increases sharply up to an absorber thickness of around 600 nm, reaching nearly 28-29%, after which it shows saturation with only marginal improvement at higher thicknesses. Similarly, the FF improves from about 78% to above 81.5% and remains relatively stable beyond 600 nm. This enhancement in PCE is attributed to increased photogenerated carrier density and higher saturation current resulting from improved light absorption at greater thicknesses [128]. However, beyond the optimal thickness, device performance begins to deteriorate, likely due to prolonged charge transport pathways that intensify carrier recombination [129]. Based on these results, an absorber thickness of 600 nm was selected for subsequent optimization studies.

Effect of series resistance

In double halide perovskite solar cell, series resistance (R_S) plays a pivotal role in determining device performance, particularly affecting the fill factor (FF) and short-circuit current density (J_{SC}). An increase in R_S leads to a reduction in FF, which in turn negatively influences JSC and overall power conversion efficiency. Consequently, a higher R_S in the fabricated device can significantly deteriorate solar cell performance. Both series and shunt resistances (R_S and R_{Sh}, respectively) are known to impact the efficiency of heterojunction and homojunction solar cells [130]. To evaluate the influence of R_S on the device parameters, the series resistance was systematically varied from 1 to 6 Ω cm². The results reveal a strong dependence of key performance metrics on R_S.

As shown in **Figure 9(a)**, the short-circuit current density (J_{SC}) remains nearly constant at around 30 mA/cm^2 up to $R_S \approx 4$ Ωcm^2, indicating that photocurrent generation and carrier collection are largely unaffected in the low-resistance regime. Meanwhile, the open-circuit voltage (V_{OC}) exhibits a slight and gradual increase with increasing R_S, suggesting minor changes in the voltage response under these conditions. In contrast, **Figure 9(b)** demonstrates that increasing R_S has a pronounced negative impact on the power conversion efficiency (PCE) and fill factor (FF). The PCE decreases steadily from approximately 28.8% to 23.2%, while the FF drops from nearly 82% to about 75% as R_S increases from 1 to 6 Ωcm^2. This degradation arises from enhanced resistive voltage losses and reduced power extraction near the maximum power point, which significantly lowers the fill factor. Thus, lowering the series resistance is crucial for sustaining a high fill factor and achieving peak performance in the proposed solar cell.

Effect of shunt resistance

Shunt resistance (R_{Sh}) is a crucial parameter governing the overall performance of photovoltaic devices. It commonly refers to the presence of shunting paths or parallel conductive channels across the p-n junction of a solar cell [131]. R_{Sh} consists of both ohmic and non-ohmic components, making its influence on device behavior more complex. **Figure 9(c)** and **Figure 9(d)** illustrates the impact of shunt resistance (R_{Sh}) on the photovoltaic performance of the $K_2LiGaBr_6$-based double-halide perovskite solar cell simulated using SCAPS-1D. Figure X illustrates the impact of shunt resistance (R_{Sh}) on the photovoltaic performance of the $K_2LiGaBr_6$-based double-halide perovskite solar cell simulated using SCAPS-1D. **Figure 9(c)** shows the variation of the short-circuit current density (J_{SC}) and open-circuit voltage (V_{OC}) as a function of R_{sh}. It is evident that J_{SC} remains nearly constant at approximately 33 mA/cm^2 throughout the investigated range, indicating that photogeneration and charge collection are largely unaffected by shunt leakage pathways. Likewise, V_{OC} exhibits only a slight improvement, gradually stabilizing around 0.99 V once R_{sh} exceeds 2000 Ωcm^2. In contrast, **Figure 9(d)** demonstrates that increasing R_{Sh} from 1000 to 6000 Ωcm^2 leads to a noticeable enhancement in both the power conversion efficiency (PCE) and fill factor (FF). The PCE rises from approximately 24.7% to 27.1%, while the FF improves from nearly 77% to above 82%. Higher shunt resistance effectively suppresses charge-carrier losses, thereby improving the overall efficiency of the simulated solar cell. At an R_{Sh} value of 6000 Ω cm², the device exhibits optimal performance with $V_{OC} = 0.99$ V, $J_{SC} = 33.15$ mA cm^{-2}, FF = 81.9%, and PCE = 27.1%.

View Article Online
DOI: 10.1039/D6MA00207B

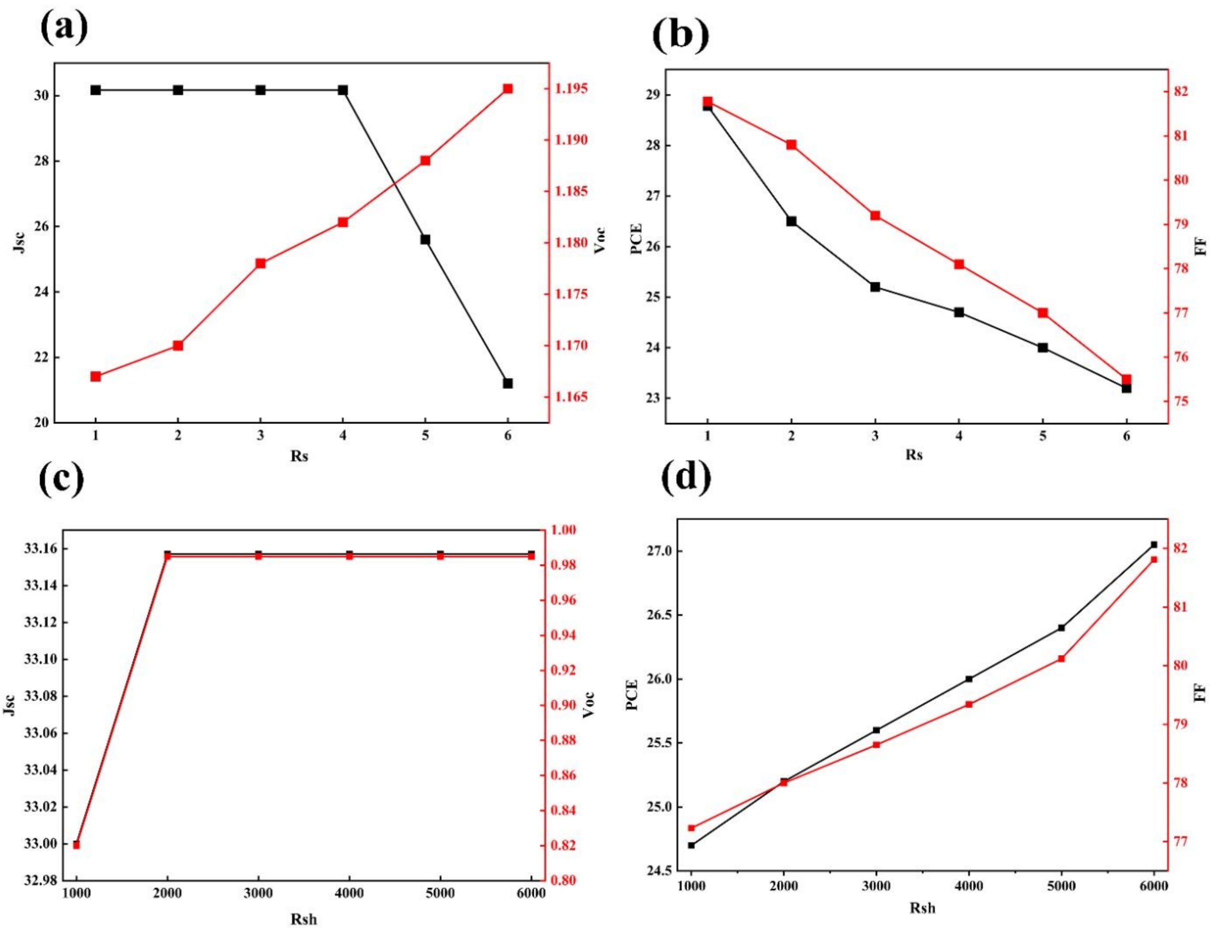

Figure 9: Effect of series resistance and shunt resistance on the simulated photovoltaic performance parameters: **(a)** variation of J_{SC} and V_{OC} with series resistance R_s, **(b)** variation of PCE and FF with series resistance R_s, **(c)** variation of J_{SC} and V_{OC} with shunt resistance R_{sh}, and **(d)** variation of PCE and FF with shunt resistance R_{sh}.

Effect of band gap variation

It is well known that the generalized gradient approximation (GGA-PBE) tends to underestimate semiconductor band gaps compared with experimental measurements and higher-level electronic structure methods [132]. To evaluate the influence of this limitation on the device-level predictions, a band-gap sensitivity analysis was performed by varying the absorber band gap over a plausible range around the calculated value while maintaining all other SCAPS input parameters constant.

As shown in **Figure 10**, increasing the absorber band gap from 1.0 to 1.6 eV resulted in a gradual increase in the open-circuit voltage (Voc) from 0.89 to 1.18 V. This behavior is consistent with the larger energetic separation between the quasi-Fermi levels achievable in wider-band-gap absorbers. In contrast, the short-circuit current density (Jsc) decreased from 35.50 to 27.10 mA cm^{-2} as the band gap increased, owing to the reduced absorption of lower-energy photons and the corresponding decrease in photogenerated charge carriers.

The fill factor (FF) exhibited only minor variations across the investigated band-gap range, remaining above 81%, indicating that charge extraction and transport characteristics were not significantly affected by moderate changes in the absorber band gap. Consequently, the power conversion efficiency (PCE) displayed a relatively broad optimum region. The efficiency increased from 25.75% at 1.0 eV to a maximum value of approximately 27.40% at 1.3 eV before gradually decreasing to 26.05% at 1.6 eV. This trend

View Article Online
DOI: 10.1039/D6MA00273

reflects the well-known trade-off between voltage enhancement and photocurrent reduction with increasing band gap.

Importantly, the simulated efficiencies remained above 25% throughout the entire investigated range, demonstrating that the overall device performance is relatively insensitive to moderate band-gap variations. The optimized $K_2LiGaBr_6$ device maintained high photovoltaic performance even when the absorber band gap was shifted by several tenths of an electronvolt from the DFT-predicted value. These results suggest that the principal device-level conclusions of this work are robust against the known band-gap underestimation associated with the PBE functional. Therefore, although quantitative efficiency values may vary slightly with more accurate band-gap corrections, the identification of $K_2LiGaBr_6$ as the more promising photovoltaic absorber remains unchanged.

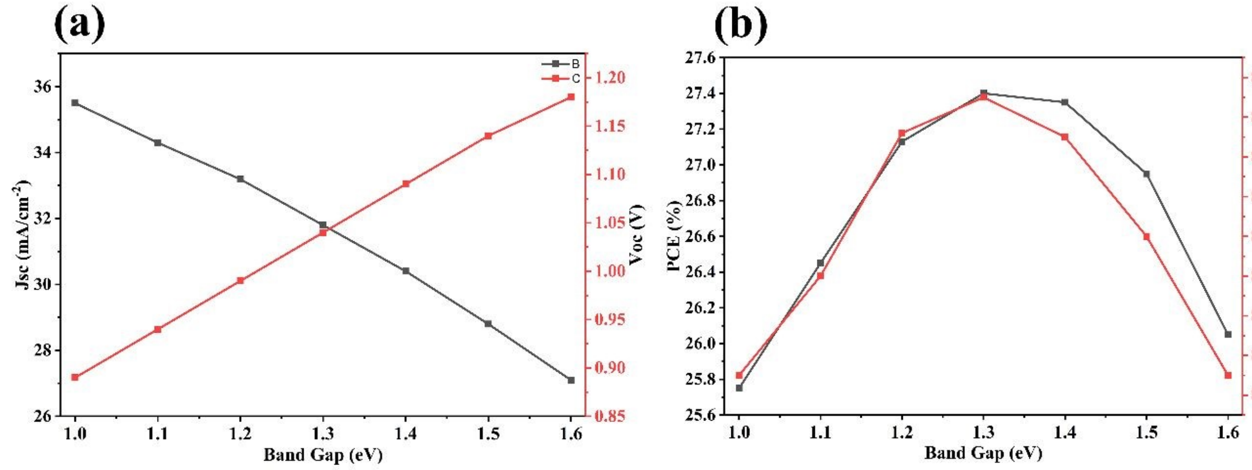

Figure 10: Effect of absorber band gap on the photovoltaic performance of the optimized $K_2LiGaBr_6$-based solar cell: **(a)** variation of J_{SC} and V_{OC} with absorber band gap, and **(b)** variation of PCE and FF with absorber band gap.

Sensitivity analysis

To evaluate the robustness of the optimized Au/MEH-PPV/$K_2LiGaBr_6$/TiO_2/FTO solar cell, a comprehensive sensitivity analysis was performed by varying carrier mobility, absorber doping concentration, bulk defect density, and interface defect density while keeping all other parameters fixed. Since experimental transport and defect characteristics for $K_2LiGaBr_6$ are currently unavailable, these simulations provide insight into the dependence of device performance on key material properties and help assess the reliability of the predicted photovoltaic efficiency.

Figure 11(a) and **Figure 11(b)** illustrate the influence of carrier mobility on the photovoltaic parameters. As the mobility increased from 1 to 100 cm² V^{-1} s^{-1}, the power conversion efficiency (PCE) improved significantly from 22.5% to 27.13%, accompanied by increases in Voc, Jsc, and FF. The enhancement originates from improved charge transport and reduced carrier accumulation within the absorber layer, which suppresses recombination losses. Beyond approximately 50 cm² V^{-1} s^{-1}, the performance gains became marginal, indicating that the device approaches a transport-saturated regime where carrier extraction is no longer the limiting factor.

The effect of absorber doping concentration is presented in **Figure 11(c)** and **Figure 11(d)**. Increasing the doping density from 10^{14} to 10^{17} cm^{-3} resulted in a gradual enhancement of Voc and FF, leading to an increase in PCE from 23.9% to 27.13%. The improved performance is attributed to stronger built-in electric fields and more efficient charge separation. Further increases in doping concentration beyond 10^{17} cm^{-3} produced only minor efficiency gains and eventually led to a slight reduction in Jsc, suggesting enhanced recombination and carrier scattering at excessively high doping levels. Consequently, an absorber doping concentration around 10^{17} cm^{-3} appears optimal for maximizing device performance.

The influence of bulk defect density is shown in **Figure 12(a) and Figure 12(b)**. Device efficiency remained relatively stable at low defect concentrations but deteriorated rapidly as the defect density increased from 10^{12} to 10^{17} cm^{-3}. The PCE decreased from 27.13% to 18.95%, while Voc dropped from 0.988 V to 0.875 V. This behavior reflects the increasing Shockley-Read-Hall (SRH) recombination associated with defect states acting as carrier traps. The pronounced reduction in Voc and FF demonstrates that bulk defects strongly affect carrier lifetime and charge collection efficiency, highlighting the importance of synthesizing high-quality absorber films with minimal defect concentrations.

Figure 12(c) and **Figure 12(d)** present the dependence of device performance on interface defect density. Similar to the bulk defects, increasing the interface defect density from 10^9 to 10^{14} cm^{-2} caused substantial performance degradation, reducing the PCE from 27.13% to 19.75%. The decrease is primarily attributed to enhanced interfacial recombination at the absorber/transport-layer junctions, which impedes efficient charge extraction and lowers both Voc and FF. The results emphasize that interface engineering is equally important as bulk defect control for achieving high device efficiencies.

View Article Online
DOI: 10.1039/D6MA00207B

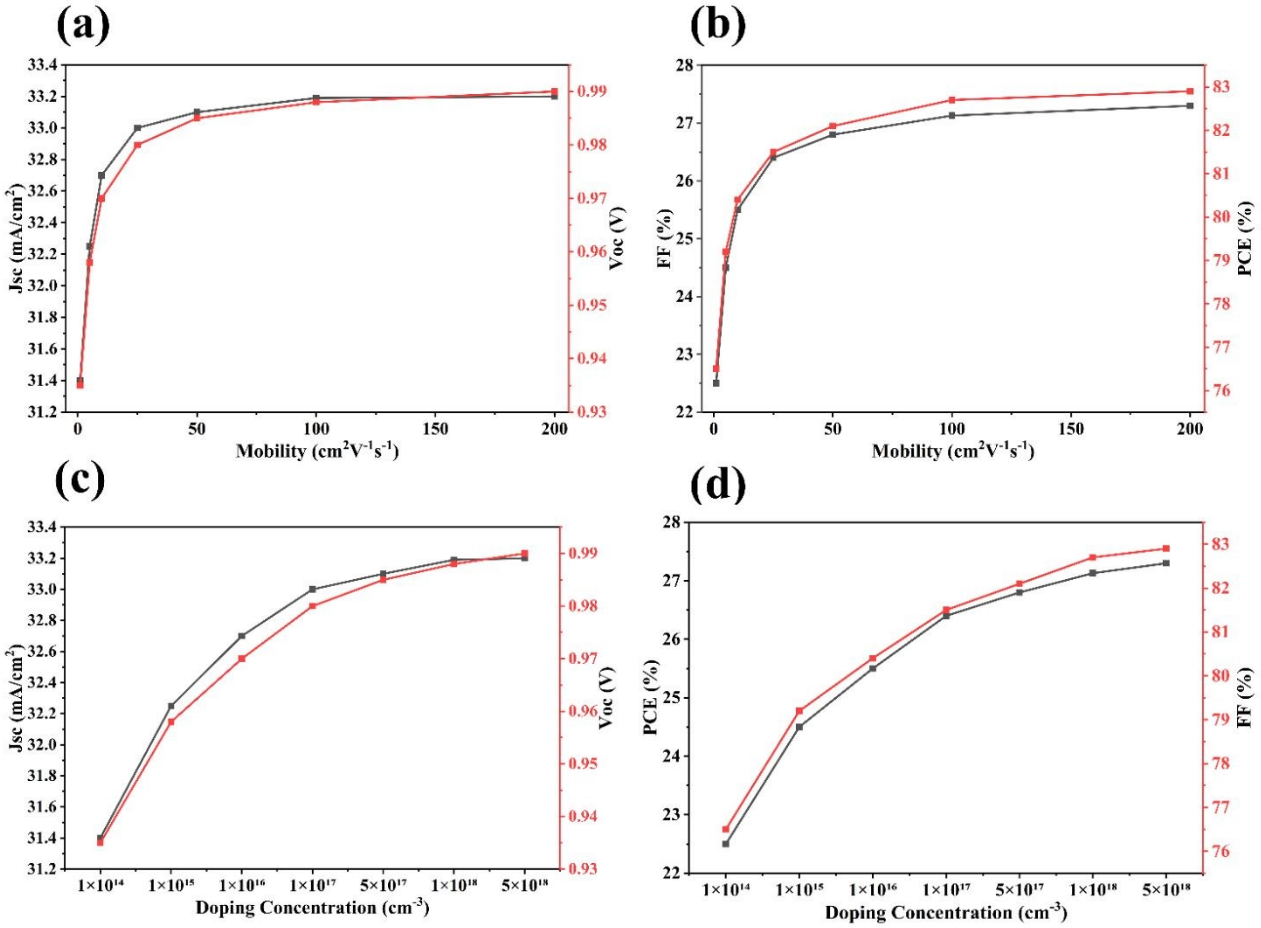

Figure 11: Variation of simulated photovoltaic performance parameters with carrier mobility and doping concentration for the **$K_2LiGaBr_6$-based solar cell**: **(a)** J_{SC} and V_{OC} as a function of carrier mobility, **(b)** FF and PCE as a function of carrier mobility, **(c)** J_{SC} and V_{OC} as a function of doping concentration, and **(d)** FF and PCE as a function of doping concentration

Overall, the sensitivity analysis demonstrates that the optimized $K_2LiGaBr_6$-based device exhibits the highest efficiency under conditions of high carrier mobility, moderate doping concentration, and low bulk and interface defect densities. Among the investigated parameters, defect densities exert the strongest influence on photovoltaic performance, whereas mobility and doping concentration mainly affect charge transport and electric-field-assisted carrier collection. These findings indicate that the reported efficiency of 27.13% represents an upper-performance scenario achievable when material quality and interface properties are carefully optimized. Because SRH recombination in SCAPS is primarily governed by bulk and interface defect states, the sensitivity analyses of defect density also provide a direct assessment of recombination-related losses within the device.

View Article Online
DOI: 10.1039/D6MA00207B

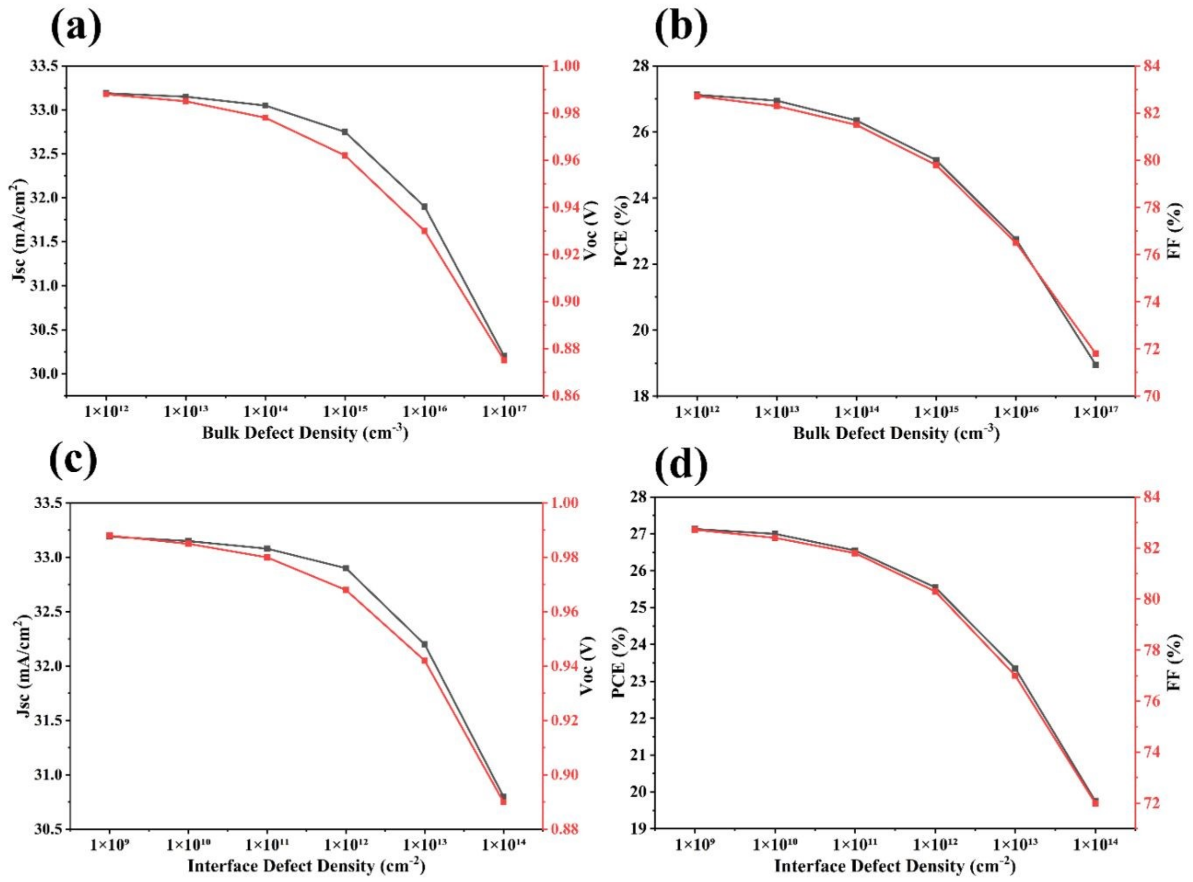

Figure 12: Effect of bulk and interface defect density on the photovoltaic performance of the **$K_2LiGaBr_6$-based solar cell**: **(a)** J_{SC} and V_{OC} as a function of bulk defect density, **(b)** FF and PCE as a function of bulk defect density, **(c)** J_{SC} and V_{OC} as a function of interface defect density, and **(d)** FF and PCE as a function of interface defect density.

Future research directions

Although this study provides a useful screening-level assessment of $K_2LiGa(Cl/Br)_6$, further theoretical and experimental validation is required before its practical photovoltaic potential can be fully established. Future work should employ higher-level electronic-structure methods, such as HSE06, mBJ, or GW calculations, to refine the predicted band gaps, band-edge positions, and optical properties beyond the known limitations of GGA-PBE. Further stability assessment is also necessary, as formation enthalpy, tolerance factor, GII, and elastic stability criteria provide only preliminary evidence of structural and mechanical feasibility; they do not confirm dynamic, thermal, chemical, moisture, or operational stability. Therefore, phonon dispersion calculations, competing phase analysis, ab initio molecular dynamics, and environmental stability tests should be pursued. Future studies should also examine defect physics and carrier dynamics in greater detail, since native vacancies, antisite defects, halide disorder, and interfacial traps may strongly influence carrier lifetime and recombination. Dedicated carrier-migration and carrier-dynamics simulations, including time-domain ab initio or nonadiabatic molecular dynamics approaches, would help clarify defect-assisted charge-loss pathways in $K_2LiGa(Cl/Br)_6$-based devices [133]. Finally, experimental synthesis, thin-film fabrication, and structural, optical, and electrical characterization are essential to verify whether $K_2LiGaBr_6$ is suitable for single-junction photovoltaic devices and whether $K_2LiGaCl_6$ is better suited for UV-sensitive or tandem-related applications.

View Article Online
DOI: 10.1039/D6MA00207B

Conclusion

This study presents a combined first-principles and SCAPS-1D device-level assessment of the lead-free double-halide perovskites $K_2LiGaCl_6$ and $K_2LiGaBr_6$ as potential photovoltaic absorbers. Density functional theory calculations confirm that both compounds are thermodynamically and mechanically stable in the cubic elpasolite structure and exhibit direct band-gap semiconducting behavior with tunable optoelectronic properties through halide substitution. Optical analysis indicates strong visible-light absorption for $K_2LiGaBr_6$, which exhibits a narrower band gap of 1.19 eV, while the wider band gap of $K_2LiGaCl_6$ (2.53 eV) suggests suitability for UV or tandem photovoltaic applications. Device simulations further reveal that optimized solar-cell architectures can achieve power conversion efficiencies reaching 27.13%, highlighting the strong coupling between intrinsic material properties and device design. Among the two candidates, $K_2LiGaBr_6$ emerges as the more promising absorber due to its favorable band gap, reduced recombination losses, and superior voltage characteristics. Overall, this multiscale computational framework provides a rational design strategy for identifying sustainable, lead-free perovskites and offers clear guidance for experimental validation and further materials optimization toward next-generation photovoltaic technologies.

References

1 Y. Akeb, A. T. Khodja, S. A. Boussaa, S. Drablia and R. Boulechfar, *Chem. Phys.*, 2025, 112832.

2 I. López-Fernández, D. Valli, C. Wang, S. Samanta, T. Okamoto, Y. Huang, K. Sun, Y. Liu, V. S. Chirvony, A. Patra, J. Zito, L. De Trizio, D. Gaur, H. Sun, Z. Xia, X. Li, H. Zeng, I. Mora-Seró, N. Pradhan, J. P. Martínez-Pastor, P. Müller-Buschbaum, V. Biju, T. Debnath, M. Saliba, E. Debroye, R. L. Z. Hoye, I. Infante, L. Manna and L. Polavarapu, *Adv. Funct. Mater.*, 2024, **34**, 2307896.

3 B. Li, F. Tian, X. Cui, B. Xiang, H. Zhao, H. Zhang, D. Wang, J. Li, X. Wang and X. Fang, *Nanomaterials*, 2022, **12**, 1773.

4 P. Zhao, Z. Cai, L. Wu, C. Zhu, L. Li and X. Wang, *J. Adv. Ceram.*, 2021, **10**, 1153–1193.

5 S. Kumar, V. Sharma, N. Kumari, G. A. Kaur, A. Saha, S. Thakur and M. Shandilya, *Ionics*, 2024, **30**, 5159–5188.

6 A. Dubey, S. L. Sanchez, J. Yang and M. Ahmadi, *Chem. Mater.*, 2024, **36**, 2165–2176.

7 N. Mhadhbi, R. Msalmi, E. Mosconi, J. Erwann, H. Khmissi, M. Orendáč, E. Čižmár and H. Naïli, *J. Alloys Compd.*, 2024, **1007**, 176450.

8 Y. Zhang, Y. Ma, Y. Wang, X. Zhang, C. Zuo, L. Shen and L. Ding, *Adv. Mater.*, 2021, **33**, 2006691.

9 F. Zhang, Z. Ma, Z. Shi, X. Chen, D. Wu, X. Li and C. Shan, *Energy Mater. Adv.*, 2021, **2021**, 2021/5198145.

10 N. Pai and D. Angmo, *Adv. Sci.*, 2025, **12**, 2412666.

11 C. Momblona, O. Malinkiewicz, C. Roldán-Carmona, A. Soriano, L. Gil-Escrig, E. Bandiello, M. Scheepers, E. Edri and H. J. Bolink, *Apl Mater.*

12 Z. Zheng, S. Wang, Y. Hu, Y. Rong, A. Mei and H. Han, *Chem. Sci.*, 2022, **13**, 2167–2183.

13 K. Wang, Z. Jin, L. Liang, H. Bian, D. Bai, H. Wang, J. Zhang, Q. Wang and S. Liu, *Nat. Commun.*, 2018, **9**, 4544.

14 A. Liang, J. Gonzalez-Platas, R. Turnbull, C. Popescu, I. Fernandez-Guillen, R. Abargues, P. P. Boix, L.-T. Shi and D. Errandonea, *J. Am. Chem. Soc.*, 2022, **144**, 20099–20108.

15 K. Vighnesh, S. Wang, H. Liu and A. L. Rogach, *ACS Nano*, 2022, **16**, 19618–19625.

16 J. J. Yoo, S. S. Shin and J. Seo, *ACS Energy Lett.*, 2022, **7**, 2084–2091.

17 P. Gao, M. Grätzel and M. K. Nazeeruddin, *Energy Environ. Sci.*, 2014, **7**, 2448–2463.

18 Y. Ling, Z. Yuan, Y. Tian, X. Wang, J. C. Wang, Y. Xin, K. Hanson, B. Ma and H. Gao, *Adv. Mater.*, 2016, **28**, 305–311.

19 X. Zhao, T. Liu and Y. Loo, *Adv. Mater.*, 2022, **34**, 2105849.

20 J. Almutlaq, J. Yin, O. F. Mohammed and O. M. Bakr, *J. Phys. Chem. Lett.*, 2018, **9**, 4131–4138.

21 W. Xiang, S. F. Liu and W. Tress, *Energy Environ. Sci.*, 2021, **14**, 2090–2113.

22 S. Yang, W. Fu, Z. Zhang, H. Chen and C.-Z. Li, *J. Mater. Chem. A*, 2017, **5**, 11462–11482.

23 W. Ke and M. G. Kanatzidis, *Nat. Commun.*, 2019, **10**, 965.

24 Ł. Szeleszczuk, K. Mądra-Gackowska and M. Gackowski, *Phys. B Condens. Matter*, 2025, 417958.

25 Ł. Szeleszczuk, K. Mądra-Gackowska, V. B. Hacholli and M. Gackowski, *J. Phys. Chem. Solids*, 2025, 113293.

26 K. Mądra-Gackowska, M. Gackowski and Ł. Szeleszczuk, *Phys. B Condens. Matter*, 2026, 418286.

View Article Online
DOI: 10.1039/D6MA00207B

27 L. A. Frolova, D. V. Anokhin, K. L. Gerasimov, N. N. Dremova and P. A. Troshin, *J. Phys. Chem. Lett.*, 2016, **7**, 4353–4357.

28 X. Han, J. Liang, J. Yang, K. Soni, Q. Fang, W. Wang, J. Zhang, S. Jia, A. A. Martí, Y. Zhao and J. Lou, *Small*, 2019, **15**, 1901650.

29 M. S. Uddin, Md. A. Al Mashud, G. F. I. Toki, R. Pandey, M. Zulfiqar, O. Saidani, K. Chandran, M. Ouladsmane and M. K. Hossain, *J. Opt.*, 2024, **53**, 3726–3742.

30 Y. Bai, Y. Meng, M. Yang, R. Tian, J. Wang, B. Jiao, H. Pan, J. Gao, Y. Wang and K. Sun, *Nat. Commun.*, 2025, **16**, 7344.

31 A. Kumar, E. Gupta, N. Iram and A. Kumar, *Trans. Electr. Electron. Mater.*, DOI:10.1007/s42341-025-00660-6.

32 C. Shi, L. Ye, Z.-X. Gong, J.-J. Ma, Q.-W. Wang, J.-Y. Jiang, M.-M. Hua, C.-F. Wang, H. Yu, Y. Zhang and H.-Y. Ye, *J. Am. Chem. Soc.*, 2020, **142**, 545–551.

33 M. A. Amin, G. Nazir, Q. Mahmood, J. Alzahrani, N. A. Kattan, A. Mera, H. Mirza, A. Mezni, M. S. Refat and A. A. Gobouri, *J. Mater. Res. Technol.*, 2022, **18**, 4403–4412.

34 K. Zhou, B. Qi, Z. Liu, X. Wang, Y. Sun and L. Zhang, *Adv. Funct. Mater.*, 2024, **34**, 2411671.

35 M. Roknuzzaman, C. Zhang, K. Ostrikov, A. Du, H. Wang, L. Wang and T. Tesfamichael, *Sci. Rep.*, 2019, **9**, 718.

36 C. Zhang and N.-G. Park, *Commun. Mater.*, 2024, **5**, 194.

37 M. R. Filip, S. Hillman, A. A. Haghighirad, H. J. Snaith and F. Giustino, *J. Phys. Chem. Lett.*, 2016, **7**, 2579–2585.

38 Cs2AgBiX6 (X = Br, Cl): New Visible Light Absorbing, Lead-Free Halide Perovskite Semiconductors | Chemistry of Materials, https://pubs.acs.org/doi/abs/10.1021/acs.chemmater.5b04231, (accessed August 26, 2025).

39 Y. chrafih, M. Al-Hattab and K. Rahmani, *J. Alloys Compd.*, 2023, **960**, 170650.

40 M. Babaei, V. Ahmadi and S. M. Pakzad Moghadam, *Adv. Theory Simul.*, 2024, 2401024.

41 Z. Zhang, S. Wang, C. Chen, M. Sun, Z. Wang, Y. Cai, Y. Tuo, Y. Du, Z. Han and X. Yun, *J. Mater. Sci. Technol.*, 2025, **227**, 108–121.

42 W. Zhou, P. Han, X. Zhang, D. Zheng, S. Yang, Y. Yang, C. Luo, B. Yang, F. Hong, D. Wei, R. Lu and K. Han, *J. Phys. Chem. Lett.*, 2020, **11**, 6463–6467.

43 J. Yadav, A. K. Sharma, M. Kumar, P. Rajput, S. P. Patel, Hari. P. Bhasker, U. Kumar, P. K. Dhawan and D. K. Chaudhary, *Trans. Electr. Electron. Mater.*, 2025, **26**, 345–355.

44 U.-G. Jong, C.-J. Yu and Y.-H. Kye, *RSC Adv.*, 2020, **10**, 201–209.

45 M. H. Miah, M. U. Khandaker, M. J. Hossen, N. E. Ashrafi, I. Jahan, M. Shahinuzzaman, M. Nur-E-Alam, M. Y. Hanfi, M. H. Ullah and M. A. Islam, *Mater. Adv.*

46 T. Kumar, M. Kumar, A. Kumar, R. Kumar and M. Bag, *Energy Fuels*, 2025, **39**, 9185–9231.

47 S. Ahmad, S. A. Ahmad, S. H. Shah, M. Zakria and J. Feng, *Mater. Today Commun.*, 2025, **44**, 111940.

48 M. Manzoor, M. Waqas Iqbal, N. A. Noor, H. Ullah, R. Sharma and S. S. Alarfaji, *Mater. Sci. Eng. B*, 2023, **287**, 116122.

49 M. Zanib, M. W. Iqbal, M. Manzoor, M. Asghar, R. Sharma, N. N. Ahmad, S. M. Wabaidur, M. A. Habila, S. A. M. Abdelmohsen, A. M. M. Abdelbacki and I. Sadique, *Mater. Sci. Eng. B*, 2023, **295**, 116604.

50 S. Al-Qaisi, Q. Mahmood, N. A. Kattan, S. Alhassan, T. Alshahrani, N. Sfina, S. Brini, A. Hakamy, A. Mera and M. A. Amin, *J. Phys. Chem. Solids*, 2023, **174**, 111184.

51 W. Kohn, *Phys. Rev. Lett.*, 1996, **76**, 3168–3171.

52 M. S. Daw and M. I. Baskes, *Phys. Rev. Lett.*, 1983, **50**, 1285–1288.

53 J. P. Perdew, K. Burke and M. Ernzerhof, *Phys. Rev. Lett.*, 1996, **77**, 3865–3868.

54 R. K. Pingak, S. Bouhmaidi and L. Setti, *Phys. B Condens. Matter*, 2023, **663**, 415003.

55 H. J. Monkhorst and J. D. Pack, *Phys. Rev. B*, 1976, **13**, 5188–5192.

56 D. C. Liu and J. Nocedal, *Math. Program.*, 1989, **45**, 503–528.

57 F. D. Murnaghan, *Am. J. Math.*, 1937, **59**, 235.

58 M. A. Hasan, I. M. M. Rahman, M. U. Khandaker, P. K. Singh and F. I. Chowdhury, *Res.*, 2025, **2**, 100408.

59 S. S. Hussain, S. Riaz, G. A. Nowsherwan, K. Jahangir, A. Raza, M. J. Iqbal, I. Sadiq, S. M. Hussain and S. Naseem, *J. Renew. Energy*, 2021, **2021**, 1–12.

60 S. Bouazizi, W. Tlili, A. Bouich, B. M. Soucase and A. Omri, *Mater. Res. Express*, 2022, **9**, 096402.

61 I. N. Khan, M. Noman and S. T. Jan, in *2023 International Conference on Emerging Power Technologies (ICEPT)*, IEEE, 2023, pp. 1–6.

62 C. Rachidy, B. Hartiti, S. Touhtouh, S. Moujoud, F. Belhora and A. Hajjaji, *Matér. Tech.*, 2023, **111**, 507.

View Article Online
DOI: 10.1039/D6MA00207B

63 M. D. Haque, M. H. Ali, M. F. Rahman and A. Z. M. T. Islam, *Opt. Mater.*, 2022, **131**, 112678.

64 W. Yuan, G. Niu, Y. Xian, H. Wu, H. Wang, H. Yin, P. Liu, W. Li and J. Fan, *Adv. Funct. Mater.*, 2019, **29**, 1900234.

65 T. T. Tran, J. R. Panella, J. R. Chamorro, J. R. Morey and T. M. McQueen, *Mater. Horiz.*, 2017, **4**, 688–693.

66 A. B. Siad, H. Riane, M. B. Siad, F. Z. Dahou, A. Allouche and M. Baira, *J. Mater. Sci.*, 2024, **59**, 1989–2007.

67 W. Travis, E. N. K. Glover, H. Bronstein, D. O. Scanlon and R. G. Palgrave, *Chem. Sci.*, 2016, **7**, 4548–4556.

68 C. J. Bartel, C. Sutton, B. R. Goldsmith, R. Ouyang, C. B. Musgrave, L. M. Ghiringhelli and M. Scheffler, *Sci. Adv.*, 2019, **5**, eaav0693.

69 M. Sk, M. T. Islam, and Gourav, *Sci. Rep.*, 2024, **14**, 24813.

70 A. U. Haq, T. S. Ahmad, A. Ahmad, B. S. Almutairi, M. Amin, M. I. Khan, N. Ehsan and R. Sharma, *Heliyon*, 2023, **9**, e21702.

71 W. Feng, R. Zhao, X. Wang, B. Xing, Y. Zhang, X. He and L. Zhang, *J. Energy Chem.*, 2022, **70**, 1–8.

72 K. D. Miller and J. M. Rondinelli, *APL Mater.*, 2023, **11**, 101108.

73 M. W. Lufaso and P. M. Woodward, in *Bond Valences*, eds. I. D. Brown and K. R. Poeppelmeier, Springer Berlin Heidelberg, Berlin, Heidelberg, 2013, vol. 158, pp. 59–90.

74 G. H. Rao, K. Bärner and I. D. Brown, *J. Phys. Condens. Matter*, 1998, **10**, L757–L763.

75 Md. Sajidul Islam, R. Ahmed, Md. Mahamudujjaman, R. S. Islam and S. H. Naqib, *Results Phys.*, 2023, **44**, 106214.

76 P. K. Kamlesh, R. Agrawal, U. Rani and A. S. Verma, *Mater. Chem. Phys.*, 2022, **275**, 125233.

77 H.-J. Wu, Q. Yang, C.-E. Hu, Y. Cheng and G.-F. Ji, *Mater. Sci. Semicond. Process.*, 2023, **153**, 107165.

78 D. H. Chung and W. R. Buessem, *J. Appl. Phys.*, 1968, **39**, 2777–2782.

79 M. A. Hadi, Md. N. Islam and J. Podder, *RSC Adv.*, 2022, **12**, 15461–15469.

80 A. Ayyaz, S. Saidi, H. Irfan Ali, A. Khadr Alqorashi, I. Kebaili, A. El-Rayyes and Q. Mahmood, *Mater. Sci. Eng. B*, 2024, **308**, 117583.

81 Q. Long, X. Nie, S.-L. Shang, J. Wang, Y. Du, Z. Jin and Z.-K. Liu, *Comput. Mater. Sci.*, 2016, **121**, 167–173.

82 H. M. Ghaithan, Zeyad. A. Alahmed, S. M. H. Qaid and A. S. Aldwayyan, *ACS Omega*, 2021, **6**, 30752–30761.

83 O. L. Anderson and H. H. Demarest, *J. Geophys. Res.*, 1971, **76**, 1349–1369.

84 M. A. Hadi, *J. Phys. Chem. Solids*, 2020, **138**, 109275.

85 T. Seddik, G. Uğur, F. Soyalp, R. Khenata, D. Prakash, I. V. Kityk, S. A. Khan, A. Bouhemadou, S. Bin-Omran, D. P. Rai and K. D. Verma, *Superlattices Microstruct.*, 2017, **109**, 1–12.

86 D. G. Pettifor, *Mater. Sci. Technol.*, 1992, **8**, 345–349.

87 Y. Benaissa Cherif, M. Rouaighia, A. Zaoui and A. Boukortt, *Acta Phys. Pol. A*, 2017, **131**, 406–414.

88 J. Luo, A. Yang and Z. Xie, *ACS Omega*, 2021, **6**, 32408–32416.

89 D. Zhou, J. Liu, S. Xu and P. Peng, *Comput. Mater. Sci.*, 2012, **51**, 409–414.

90 Md. Lokman Ali, *Int. J. Mater. Sci. Appl.*, 2016, **5**, 202.

91 O. L. Anderson, *J. Phys. Chem. Solids*, 1963, **24**, 909–917.

92 Z. Li and R. C. Bradt, *J. Mater. Sci.*, 1987, **22**, 2557–2559.

93 S. I. Ranganathan and M. Ostoja-Starzewski, *Phys. Rev. Lett.*, 2008, **101**, 055504.

94 R. Gaillac, P. Pullumbi and F.-X. Coudert, *J. Phys. Condens. Matter*, 2016, **28**, 275201.

95 Md. B. H. Parosh, M. Saiduzzaman, J. Islam, N. J. Nisha and I. A. Ovi, *RSC Adv.*, 2025, **15**, 10085–10105.

96 A. E. Dixon, in *Solar Energy Conversion*, Elsevier, 1979, pp. 773–784.

97 Md. Tarekuzzaman, N. Shahadath, M. Montasir, O. Alsalmi, M. H. Mia, H. Al-Dmour, Md. Rasheduzzaman and Md. Z. Hasan, *RSC Adv.*, 2025, **15**, 13643–13661.

98 T.-Y. Tang, X.-H. Zhao, D.-Y. Hu and Y.-L. Tang, *Mol. Phys.*, 2022, **120**, e2018064.

99 A. B. Siad, H. Riane, M. B. Siad, F. Z. Dahou, A. Allouche and M. Baira, *J. Mater. Sci.*, 2024, **59**, 1989–2007.

100 M. Sk, M. T. Islam, and Gourav, *Sci. Rep.*, 2024, **14**, 24813.

101 H. Wu, A. Erbing, M. B. Johansson, J. Wang, C. Kamal, M. Odelius and E. M. J. Johansson, *ChemSusChem*, 2021, **14**, 4507–4515.

102 J. Luo, A. Yang and Z. Xie, *ACS Omega*, 2021, **6**, 32408–32416.

View Article Online
DOI: 10.1039/D6MA00207B

103 M. Sk, M. T. Islam, and Gourav, *Sci. Rep.*, 2024, **14**, 24813.

104 H. Ben Abdallah and W. Ouerghui, *Opt. Quantum Electron.*, 2022, **54**, 20.

105 A. Ayyaz, A. S. Alofi, S. K. Ali, S. Alotaibi, R. Anbarasan, M. S. Al-Buriahi, M. Jeridi and Q. Mahmood, *J. Phys. Chem. Solids*, 2025, **199**, 112559.

106 A. Pinchuk, U. Kreibig and A. Hilger, *Surf. Sci.*, 2004, **557**, 269–280.

107 Q.-J. Liu, N.-C. Zhang, F.-S. Liu, H.-Y. Wang and Z.-T. Liu, *Phys. Status Solidi B*, 2013, **250**, 1810–1815.

108 H. Albalawi, B. U. Haq, G. Nazir, T. Ghrib, N. A. Kattan, Q. Mahmood, A. I. Aljameel, M. Morsi and S. Bouzgarrou, *Mater. Today Commun.*, 2022, **32**, 104106.

109 J. Petzelt and I. Rychetský, in *Reference Module in Materials Science and Materials Engineering*, Elsevier, 2016, p. B9780128035818010201.

110 Y. Jiang, X. Wang and A. Pan, *Adv. Mater.*, 2019, **31**, 1806671.

111 P. Y. Yu and M. Cardona, *Fundamentals of Semiconductors*, Springer Berlin Heidelberg, Berlin, Heidelberg, 2005.

112 M. Tariq, M. A. Ali, A. Laref and G. Murtaza, *Solid State Commun.*, 2020, **314–315**, 113929.

113 L. N. Quan, B. P. Rand, R. H. Friend, S. G. Mhaisalkar, T.-W. Lee and E. H. Sargent, *Chem. Rev.*, 2019, **119**, 7444–7477.

114 N.-G. Park, *Mater. Today*, 2015, **18**, 65–72.

115 M. Fatmi, K. Bouferrache, M. A. Ghebouli, B. Ghebouli, F. K. Alanazi, M. D. Albaqami, S. Mohammad and A. Benali, *Sci. Rep.*, 2025, **15**, 20851.

116 M. Palummo, E. Berrios, D. Varsano and G. Giorgi, *ACS Energy Lett.*, 2020, **5**, 457–463.

117 X. Huang, Y. Wang, Y. Weng, Z. Yang and S. Dong, *Phys. Rev. Mater.*, 2020, **4**, 104601.

118 Y. Yuan, G. Yan, R. Hong, Z. Liang and T. Kirchartz, *Adv. Mater.*, 2022, **34**, 2108132.

119 E. J. Juarez-Perez, M. Wuβler, F. Fabregat-Santiago, K. Lakus-Wollny, E. Mankel, T. Mayer, W. Jaegermann and I. Mora-Sero, *J. Phys. Chem. Lett.*, 2014, **5**, 680–685.

120 T. M. Brenner, D. A. Egger, L. Kronik, G. Hodes and D. Cahen, *Nat. Rev. Mater.*, 2016, **1**, 15007.

121 M. Fox and G. F. Bertsch, *Am. J. Phys.*, 2002, **70**, 1269–1270.

122 P. Y. Yu and M. Cardona, *Fundamentals of Semiconductors: Physics and Materials Properties*, Springer Berlin Heidelberg, Berlin, Heidelberg, 2010.

123 M. Dressel, G. Gruener and G. F. Bertsch, *Am. J. Phys.*, 2002, **70**, 1269–1270.

124 L. M. Pazos-Outón, T. P. Xiao and E. Yablonovitch, *J. Phys. Chem. Lett.*, 2018, **9**, 1703–1711.

125 M. Al-Hattab, L. Moudou, M. Khenfouch, O. Bajjou, Y. Chrafih and K. Rahmani, *Sol. Energy*, 2021, **227**, 13–22.

126 S. Porwal, M. Paul, H. Dixit, S. Mishra and T. Singh, *Adv. Theory Simul.*, 2022, **5**, 2200207.

127 S. Srivastava, R. Srivastava, D. Punetha, A. K. Sharma and Y. K. Prajapati, *Chem. Phys. Lett.*, 2024, **854**, 141557.

128 M. S. Uddin, M. K. Hossain, M. B. Uddin, G. F. I. Toki, M. Ouladsmane, M. H. K. Rubel, D. I. Tishkevich, P. Sasikumar, R. Haldhar and R. Pandey, *Adv. Electron. Mater.*, 2024, **10**, 2300751.

129 S. Khatoon, V. Chakraborty, S. K. Yadav, S. Diwakar, J. Singh and R. B. Singh, *Sol. Energy*, 2023, **254**, 137–157.

130 M. U. N. Tariq, M. Kashif and M. Malik, *J. Opt.*, 2024, 1–15.

131 Y. He, L. Xu, C. Yang, X. Guo and S. Li, *Nanomaterials*, 2021, **11**, 2321.

132 M. K. Choudhary, A. R. V, G. S. S and P. Ravindran, *Adv. Theory Simul.*, 2025, **8**, e00771.

133 W. Li, J. Liu, F.-Q. Bai, H.-X. Zhang and O. V. Prezhdo, *ACS Energy Lett.*, 2017, **2**, 1270–1278.

View Article Online
DOI: 10.1039/D6MA00207B

Data availability

Data will be made available upon request.